Astron. Astrophys. 361, 121–138 (2000)

ASTRONOMY
AND
ASTROPHYSICS

Low and high frequency quasi-periodic oscillations in 4U1915-05

L. Boirin[1], **D. Barret**[1], **J.F. Olive**[1], **P.F. Bloser**[2], **and J.E. Grindlay**[2]

[1] Centre d'Etude Spatiale des Rayonnements, CNRS/UPS, 9 Avenue du Colonel Roche, 31028 Toulouse Cedex 04, France (boirin@cesr.fr)
[2] Harvard Smithsonian Center for Astrophysics, 60 Garden Street, Cambridge, MA 02138, USA

Received 1 October 1999 / Accepted 6 July 2000

Abstract. The X-ray burster and dipper 4U1915-05 (also known as XB1916-053) was observed 19 times for a total exposure of roughly 140 ks between 1996 February and October with the proportional counter array (PCA) aboard *Rossi X-ray Timing Explorer* (RXTE). We present here the detailed timing study of its X-ray emission. The source was observed in both a high intensity/soft spectral and a low intensity/hard spectral state. The 2-20 keV luminosities are about 1.4×10^{37} and 3.2×10^{36} ergs s^{-1} in the two regimes respectively (assuming a source distance of 9.3 kpc). We confirm that 4U1915-05 is an atoll source based on its spectral behaviour and its aperiodic variability in the frequency range $\sim 4 \times 10^{-3} - 128$ Hz. 4U1915-05 displays red noise below $\sim$ 1 Hz, but is especially remarkable for its quasi-periodic variability detected for the first time at several timescales. We detect low frequency quasi-periodic oscillations (LFQPOs) between $\sim$ 5 and 80 Hz, as well as high frequency QPOs (HFQPOs) between $\sim$ 200 and 1300 Hz. Both LFQPOs and HFQPOs frequencies positively correlate with the mass accretion rate inferred from the position of the source on the color-color diagram. In a narrow range of luminosity, we also detect twin simultaneous HFQPOs separated by 348 ± 12 Hz.

Key words: stars: individual: 4U1915-05 – stars: neutron – X-rays: stars

1. Introduction

1.1. High frequency quasi-periodic oscillations in low-mass X-ray binaries

One of the greatest successes of RXTE is the discovery of HFQPOs in the X-ray emission of low-mass X-ray binaries (LMXBs). RXTE made it possible by the combination of the large effective area of the PCA, an excellent time resolution, an extended telemetry bandwidth and optimized observing efficiency. HFQPOs ranging from $\sim$ 300 to $\sim$ 1200 Hz have been reported so far from 21 neutron star LMXBs (Van der Klis 1999): the 6 Z sources, 12 known atoll sources, the unknown bursting source in the galactic center region, the recently discovered X-ray bursters XTE J2123-058 and XTE J1723-376 (Marshall & Markwardt 1999). Following their discoveries, it has been realized that they could possibly be used to constrain the fundamental parameters of neutron stars, such as their spin periods, their masses, and their radii. Implications of general relativity in the interpretation of these HFQPOs have also been discussed by several authors like, e.g., Kaaret et al. (1997), Kluźniak (1998), Miller et al. (1998b).

In most systems, twin HFQPOs are observed with a separation in the range 220-360 Hz. Changes in the source luminosity cause the twin peaks to shift simultaneously in a way that their separation remains approximatively constant. For the Z source Sco X-1 and the atoll sources 4U1608-52, 4U1728-34 and 4U1735-44, however, the frequency separation significantly decreases as the HFQPOs frequencies increase (Van der Klis et al. 1997; Méndez et al. 1998c; Méndez & Van der Klis 1999; Ford et al. 1998b; Psaltis et al. 1998). In a few X-ray bursters (e.g. 4U1702-43, KS1731-260), which are atoll sources, coherent pulsations have been seen during type I X-ray bursts at frequencies equal or twice the frequency difference between the twin HFQPOs (Markwardt et al. 1999; Smith et al. 1997). In 4U1636-53 and 4U1728-34, burst oscillations have been detected at a frequency significantly greater than the twin HFQPOs separation (Méndez et al. 1998a; Méndez & Van der Klis 1999).

Specific also to the atoll sources, HFQPOs are detected when the source is in the so-called island state and on the lower branch of the banana state. These two states are easily identified in color-color diagrams and there is conclusive evidence that the accretion rate increases from the island to the banana state (Hasinger & Van der Klis 1989). They are associated with different types of power density spectra (PDS) at low frequencies (in the remainder of this paper we define low frequencies as frequencies below 100 Hz). In the island state, the source displays high frequency noise (HFN also called "flat topped noise") and the PDS can be approximated by a zero-centered Lorentzian (Olive et al. 1998, for 1E1724-3045), or alternatively by broken power laws (Wijnands & Van der Klis 1999a, for example). Superposed to the noise, a QPO-like feature is generally seen around $\sim 0.5 - 70$ Hz (see Table 1 for a review). In this state, the root mean square (RMS) values of the fluctuations (to the mean flux) reach 50% (Van der Klis 1994). On the other hand,

Send offprint requests to: L. Boirin

Table 1. Sources for which a QPO (or a QPO-like feature or peaked HFN) has been reported in addition to either flat topped noise or red noise in their low frequency ($\sim 10^{-3} - 100$ Hz) PDS.

Source	Type[a]	Flat topped noise and QPO	References[b]	Red noise and QPO	References[b]
4U 0614+09	A	Y	1[c], 2	Y	44[c], 45
4U 1608-52	A	Y	3, 4, 5, 2	-	
4U 1702-42	A	-		Y	14[c]
4U 1705-44	A	Y	6, 5, 7	Y	5[c]
1E 1724-30	A	Y	8, 9	-	
4U 1728-34	A	Y	10, 11	-	
KS 1731-260	A	-		Y	15, 9
4U 1735-44	A	Y	2	Y	16
SLX 1735-269	A	Y	12, 9	-	
4U 1744-26	A	-		Y	17, 18
XTE J1806-246	-[d]	-		Y	19, 20
SAX J1808.4-3658	P	Y	13	-	
GX 13+1	A	-		Y	21
4U 1812-12	A	Y	2	-	
4U 1820-30	A	-		Y	22
GS 1826-238	A	Y	9	-	
4U 1915-05	A	-		Y	46
XTE J2123-058	A	-		Y	23, 24
Sco X-1	Z	Y	25, 2	Y	25, 26, 27
GX 340+0	Z	Y	2	Y	28
GX 349+2	Z	-		Y	29
GX 5-1	Z	Y	2	Y	30, 31, 32
GX 17+2	Z	Y	2, 33	Y	33, 34, 35
Cyg X-2	Z	Y	2, 36, 37, 38	Y	36, 37, 38, 39
Cir X-1	Z[e]	Y	40, 41, 42, 43	Y	40, 42, 43

[a] A, atoll source; Z, Z source; P, millisecond X-ray pulsar.
[b] See Van Paradijs (1995) for complementary references up to 1995.
[c] After the power spectra published in the literature.
[d] Both atoll and Z classifications have been proposed (Wijnands & Van der Klis 1999b; Revnivtsev et al. 1999).
[e] Shirey et al. (1998; 1999)

References: (1) Méndez et al. (1997); (2) Wijnands and Van der Klis (1999a); (3) Yoshida et al. (1993); (4) Yu et al. (1997); (5) Berger and Van der Klis (1998); (6) Hasinger and Van der Klis (1989); (7) Ford et al. (1998a); (8) Olive et al. (1998); (9) Barret et al. (2000); (10) Strohmayer et al. (1996); (11) Ford and Van der Klis (1998); (12) Wijnands and Van der Klis (1999c); (13) Wijnands and Van der Klis (1998); (14) Markwardt et al. (1999); (15) Wijnands and Van der Klis (1997); (16) Wijnands et al. (1998c); (17) Lewin et al. (1987); (18) Strohmayer (1998); (19) Wijnands and Van der Klis (1999b); (20) Revnivtsev et al. (1999); (21) Homan et al. (1998); (22) Wijnands et al. (1999); (23) Homan et al. (1999); (24) Tomsick et al. (1999); (25) Van der Klis et al. (1997); (26) Van der Klis et al. (1996); (27) Dieters and Van der Klis (2000); (28) Jonker et al. (1998); (29) Kuulkers and Van der Klis (1998); (30) Kamado et al. (1997); (31) Wijnands et al. (1998b); (32) Vaughan et al. (1999); (33) Kuulkers et al. (1997); (34) Wijnands et al. (1996); (35) Wijnands et al. (1997a); (36) Wijnands et al. (1997b); (37) Kuulkers et al. (1999); (38) Focke (1996); (39) Wijnands et al. (1998a); (40) Oosterbroek et al. (1995); (41) Shirey et al. (1996); (42) Shirey et al. (1998); (43) Shirey et al. (1999); (44) Ford et al. (1997); (45) Ford (1997); (46) This paper.

on the banana branch, the shape of the PDS is roughly a power law with an index of -1.0; the so-called very low frequency noise (VLFN) or red noise (Hasinger & Van der Klis 1989). In this state, the RMS is around 10% or less. In the lower part of the banana branch, a broad structure, often refered to as "peaked HFN", or a QPO is seen at frequencies in the range 1-70 Hz (see Table 1). A correlation between the centroid frequency of the bump, and the frequency of the upper kHz QPO has been found in several LMXBs (e.g. KS1731-260), and interpreted in the framework of a Lense-Thirring effect (Stella & Vietri 1998; Stella et al. 1999) or a two-oscillator model (Titarchuk & Osherovich 1999; Osherovich & Titarchuk 1999a).

1.2. 4U1915-05

In the context of these results, we have analyzed our RXTE observations of the type I X-ray burster 4U1915-05. This source is known as the first dipping X-ray source discovered, providing the first reliable evidence for the binary nature of such sources (Walter et al. 1982; White & Swank 1982; Swank et al. 1984; Smale et al. 1988).

The period of the dips in X-rays is 50 minutes, the shortest among dipping sources (White & Swank 1982; Walter et al. 1982; Yoshida et al. 1995; Chou et al. 1999). It is also optically identified with a 21st V magnitude blue star (Grindlay et al. 1988). A modulation is seen in the optical

Table 2. Observation log. We list the name assigned to the observation, its start and stop times (day and UT hour), the number of PCUs working (P), the high time resolution data modes M available (G, E and CB designate the E_125us_64M_0_1s, GoodXenon_16s and CB_2ms_64M_0_249 (Binned Burst Catcher) configurations respectively), the total exposure time (T_{total}) in seconds after screening (on elevation and offset), the number of bursts (B) and dips (D) present, the exposure time in seconds of the persistent light curve after filtering out the bursting and dipping parts (T) and the 2-20 keV background subtracted count rate in units of cts s^{-1} PCU^{-1} (R) of the persistent emission. $^{(1)}$ Gain epoch 1 data (the other observations are gain epoch 3). ^{a} Two small observations were carried out on May 23rd, we merged them together for clarity.

Name	Start		End		P	M	T_{total}	B	D	T	R
02/10$^{(1)}$	Feb. 10	00:14:04	Feb. 10	05:09:13	5	G	6750	0	3	4112	73.0
03/13$^{(1)}$	March 13	22:41:24	March 14	00:54:13	5	G	3316	0	0	2880	97.1
05/05	May 5	05:59:39	May 5	09:46:13	3, 4	G	4039	0	0	3904	68.7
05/06	May 5	22:16:00	May 6	03:37:13	4	G, CB	6912	1	0	6592	62.1
05/14	May 14	09:22:05	May 14	12:55:13	3	E	7599	0	3	4432	29.5
05/15	May 15	12:32:06	May 15	15:11:13	3	E	6622	0	0	6592	41.5
05/16	May 16	12:56:45	May 16	16:31:13	3	E	7955	0	4	5936	42.6
05/17	May 17	08:20:08	May 17	11:49:13	3	G	7640	0	4	2864	35.4
05/18	May 18	09:53:47	May 18	13:20:13	3	E	7495	0	4	3168	21.7
05/19	May 19	10:06:38	May 19	13:37:13	3	E	7389	0	2	2560	22.6
05/20	May 20	06:50:10	May 20	10:16:13	3	E	7496	0	2	3904	25.2
05/21	May 21	07:47:52	May 21	11:22:13	3	E	7949	0	4	2400	23.3
05/22	May 22	12:37:55	May 22	16:26:13	3	E	8624	0	6	3584	27.6
05/23^{a}	May 23	07:50:56	May 23	11:20:13	4, 5	E	7723	0	8	4128	39.8
06/01	June 1	17:36:53	June 1	21:36:13	5	E, G, CB	9336	1	4	4544	46.3
07/15	July 15	11:49:45	July 15	16:24:13	5	E	9786	0	6	5168	33.9
08/16	Aug. 16	10:37:49	Aug. 16	14:55:13	4, 5	E	9983	1	5	6384	28.1
09/06	Sept. 6	15:57:13	Sept. 6	21:26:13	5	E	9344	0	1	6032	39.5
10/29	Oct. 29	06:53:21	Oct. 29	11:53:13	5	E	9464	1	2	5120	35.9

but at a period $\sim$ 1% larger than the X-ray dip period (Callanan et al. 1995). The discrepancy between the two periods is confirmed by Chou et al. (1999) who combined historical and recent data (including the RXTE data used in this paper). This discrepancy has led to several interpretations among which the SU UMa[1] model is prefered, although the hierarchical triple system model proposed by Grindlay et al. (1988) is still possible (Chou et al. 1999).

To date, the only timing study of the non-dipping and non-bursting emission of 4U1915-05 was carried out with the Ginga data, which represented the most extensive X-ray observations of the source before the launch of BeppoSAX and RXTE. The 1-37 keV luminosity varied between 5×10^{36} and 1.2×10^{37} ergs s^{-1}, in the range of luminosities previously observed for the source. A V-shape was observed in the hardness (7-18/1-7 keV) intensity (1-18 keV) diagram (Yoshida 1992). The $3 \times 10^{-3} - 1$ Hz PDS were fitted with a power law of index -0.6 for the left branch of the V data and of index roughly -1.1 for the right branch data. Yoshida (1992) suggested that 4U1915-05 was an atoll source. Yoshida (1992) interpreted the left branch of the hardness intensity diagram as the island state and the right branch as the banana state, although the two branches overlapped in the color-color diagram.

From an X-ray burst showing photospheric radius expansion in the GINGA data, the distance to the source was estimated as 9.3 kpc (Yoshida 1992). 4U1915-05 was observed at energies up to 100 keV by BeppoSAX (Church et al. 1998). This was the first observation of a hard X-ray tail in the spectrum of 4U1915-05. Indeed, previous pointed and monitoring observations at high energies with OSSE and BATSE aboard the Compton Gamma-Ray Observatory had failed to detect the burster (Barret et al. 1996; Bloser et al. 1996). 4U1915-05 is the first dipping source to belong to the growing group of LMXBs detected up to ~ 100 keV (Barret et al. 2000).

In this paper we report on the timing analysis of the X-ray emission which led to the discovery of HFQPOs and LFQPOs in 4U1915-05. In the next section, we describe the observations and the data analysis. Then, we present the results. Finally, we compare 4U1915-05 to similar sources and discuss the results in the framework of currently proposed models of HF and LFQPOs.

2. Observations and data analysis

2.1. The RXTE/PCA observations

4U1915-05 was observed by RXTE on 19 occasions in 1996: on February 10th, March 13th, May 5-6th, May 14th to 23rd, June 1st, July 15th, August 16th, September 6th and October 29th. The log of the observations is presented in Table 2. An observation has an exposure time of roughly 8000 seconds and is provided as typically three data files with gaps between files.

[1] SU UMa stars are cataclysmic variables, which during their long ('super') outbursts show humps which have a period which is a few% longer than their orbital period.

These files are refered as segments of observation in our analysis. We report on the data collected in the 2-60 keV range with the PCA. It consists of 5 nearly identical large area Proportional Counter Units (PCU 0 to 4) corresponding to a total collecting area of ~ 6500 cm^2 (Jahoda et al. 1996). For safety reasons, PCUs are switched on and off in the course of an observation. During our observations, the data were mainly obtained in three different PCU configurations: all PCUs on, first four on and first three on. Furthermore, our observations cover two PCA gain epochs: the February 10th and March 13th observations belong to the first one whereas the following observations belong to the third one. Different response matrices were used for each set. More than 138 ks of good data are available after recommended screening (elevation angle above the Earth's limb greater than 10 degrees and pointing offset angle less than 0.02 degree).

The all-sky monitor (ASM) aboard RXTE consists of three coded-aperture cameras mounted on a motorized rotation drive, allowing to view different regions of the sky during a satellite orbit (Levine et al. 1996). The instrument is sensitive in the energy range $\sim$ 2-12 keV. Fig. 1 is the ASM light curve of 4U1915-05 during 1996. The binning time is one day. The times of the PCA observations are flagged with arrows. Four X-ray bursts were recorded during the PCA observations: on May 5th, June 1st, August 16th and October 29th. With the exception of the first one, they began during a dip. A total of 58 primary or secondary dips (or parts of dips) were observed, lasting typically 400 seconds. Dips are thought to be due to occultation of the internal emitting region by vertical structure at the outer edge of the accretion disk (Walter et al. 1982; White & Swank 1982). Primary dips occur at intervals consistent with an orbital period of $\sim$ 50 minutes. Secondary dips are "anomalous" dips, narrower than the primary ones. They occur irregularly at $\sim 180^\circ$ out of phase with the primary dips (Chou et al. 1999). Dipping is almost 100% in the 3-5 keV energy range, but only $\sim$ 65% in the 5-30 keV range.

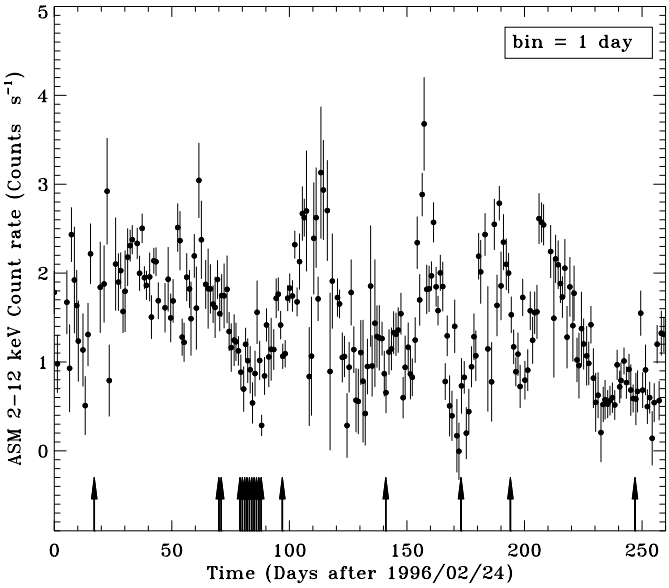

Fig. 1. Light curve of 4U1915-05 as observed by the RXTE/ASM. The binning time is one day. The times of the pointed observations are indicated by arrows.

2.2. Data modes

The *Standard 2* mode is available for each observation. This mode provides counts integrated during 16 seconds in 128 energy channels covering the 2-60 keV energy range. The high time resolution data were provided in two different modes, depending on the observations (see Table 2): the E_125s_64M_0_1s mode with 122 μs resolution or the GoodXenon_16s mode with ~ 1 μs resolution. The bursts that occured on October 29th and August 16th were recorded in the 122 μs resolution mode. The bursts that occured on May 5th and June 1st were recorded during 3.75 seconds in a burst catcher mode with 2 ms resolution.

2.3. Data analysis

2.3.1. Light curves, color-color and hardness-intensity diagrams

For the light curves, color-color and hardness-intensity diagrams, we have used the *Standard 2* mode data. We made light curves in adjacent energy bands. The bursts and dips were then filtered out after visual screening of the light curves to generate the color-color and hardness-intensity diagrams for the persistent emission. The soft color was calculated as the 3-5 keV/1.7-3 keV count rate ratio, and the hard color as 10-30 keV/5-10 keV.

As all the PCUs have different energy responses, the absence of a PCU can mimic spectral variations. Thus, we used the data collected with the first three PCUs since they were continuously operating during all our observations.

Differences between response matrix of gain epoch 1 and 3 introduce differences in the boundaries of the energy channels used. This instrumental effect introduces shifts between the colors or count rates obtained from different epochs. We quantified these shifts using the Crab nebula which is a steady source. We find that the correction factors to apply to gain epoch 1 data in order to make them match the epoch 3 region are +10.1%, -1.5%, -1.1% and +2.8% for the count rates in the energy bands 1.7-3, 3-5, 5-10 and 10-30 keV respectively. The correction factors are -10.5% and +4.0% for the soft and hard colors respectively. We applied these correction factors to 4U1915-05 data.

2.3.2. Power density spectra

To investigate the variability of 4U1915-05, we computed PDS using the FTOOLS *powspec*. We treated separately the data obtained from the different high time resolution modes.

To reach timescales ranging from roughly 10 ms to 4 minutes, the data were rebinned to a ~ 4 ms resolution. Then, each continuous set was divided into segments of 65536 bins. A fast Fourier transform (FFT) of each segment was computed yielding a low frequency PDS in the range $\sim 4 \times 10^{-3} - 128$ Hz.

To reach timescales ranging from roughly 0.25 ms to 1 second, the data were rebinned to a $\sim$ 122 μs resolution. Each

continuous set was divided into segments of 8192 bins. A FFT of each segment was computed leading to high frequency PDS in the range 1-4096 Hz. Then, the low or high frequency PDS obtained from a given set of observations, a given observation or a given segment of observation were averaged together to obtain a final PDS representative of the set, observation or segment.

The PDS were normalized according to Leahy et al. (1983) so that the average power expected from a Poisson distribution is 2. We have checked in the high frequency PDS that the average white noise level above 1500 Hz was indeed 2, indicating that deadtime corrections were not needed.

The error on each PDS bin has been set to $E_P = \frac{P_m}{\sqrt{MW}}$ where M is the number of raw PDS averaged together, W the number of raw frequency bins averaged together (Van der Klis 1989). P_m is set to the Fourier power at the point considered for low frequency PDS (where the power can differ significantly from the white noise level 2 because of the source aperiodic variability) and to 2 for the high frequency PDS. Both logarithmic and linear rebinnings were applied.

Different components were summed to fit the resulting PDS: a constant for the white noise level (C), a power law for the VLFN (PL), a cutoff power law for the HFN (CPL). The functional shapes used for the latter components are $A\nu^{\alpha}$ and $A\nu^{\alpha}\exp(-\nu/\nu_{\rm cutoff})$ respectively, where A is the normalization, α the power law index, ν the frequency and $\nu_{\rm cutoff}$ the cutoff frequency. C is a free parameter for the high frequency PDS and is set to 2 for the low frequency PDS. We used Gaussians (G) to describe the QPO features. Note that Lorentzians are also currently used (Van der Klis 1995).

All the fits were performed using a χ^2 minimization technique. The errors on the analytic model parameters correspond to a χ^2 variation of 2.7, equivalent to the 90% confidence region for a single interesting parameter.

To compute the RMS, the PDS were normalized according to Belloni and Hasinger (1990) taking into account the total and background count rates. The RMS was then obtained by integrating the normalized PDS in the appropriate frequency range.

We have also computed PDS of data from the bursts. For the bursts recorded in the 122 μs resolution mode, we have calculated an FFT power spectrum using 4096 bins lasting 244 μs, so that one PDS corresponds to a segment of the burst of 1 sec duration and the Nyquist frequency is 2048 Hz. For the other bursts, the time resolution is only $\sim$ 2 ms, yielding a Nyquist frequency of 256 Hz.

2.3.3. Search technique for quasi-periodic oscillations

To look for weak QPOs in the PDS (as in the case of 4U1915-05), we developed an algorithm which computes for each PDS the width of the window which maximises the signal to noise ratio (SNR) within the window. Assuming that a given window of width w contains N frequency bins, the error on the binned points becomes $E_P = \frac{P_m}{\sqrt{MWN}}$ and the SNR can be computed as:

$$SNR(in\ \sigma) = \frac{\frac{1}{N}\sum P_j - P_{ref}}{E_P} \quad (1)$$

where P_j are the N PDS points contained in the window of width w and P_{ref} is the reference power. For the low frequency PDS, given the weakness of the VLFN component above $\sim$ 1 Hz, we looked for excesses above P_{ref}=2, the theoretical level expected from Poissonian noise. PDS have been processed through the algorithm and searched for excesses of widths from 1 to 50 Hz in the frequency range 1-100 Hz. For the high frequency PDS, we looked for excesses of widths 5-200 Hz in the frequency range 100-1500 Hz. We used the noise level averaged above 1500 Hz ($\sim$ 2.0) as the reference P_{ref} for the search of excesses in the PDS. In both cases, we first selected the positive detections above 3.5 σ. A new significance level inferred from the fit was then attributed to each excess in order to take into account the excess shape. We report here on the LFQPOs and HFQPOs which have a significance level greater than 3 σ. This significance level is reported in Table 4 with the properties of the QPOs detected in 4U1915-05. We do mention either the observation or the segments, so that no overlapping is possible.

This algorithm does not take into account the number of trials in determining the significance level. To determine the real significance of the detections, we follow Van der Klis (1989) and define the $(1-\epsilon)$ confidence level P_{detect} as the power level that has only the small probability ϵ/N_{trial} to be exceeded by a noise power. N_{trial} is the number of different power values that one wishes to compare with P_{detect}. It may be the total number of bins in the PDS, or less if only a given frequency range is looked for excesses. The number of different PDS looked at may also be included in the number of trials but we did not take it into consideration. In our case, the high frequency PDS are scanned over a frequency range of 1400 Hz. The exposure time of a raw PDS is 1 second (corresponding to a frequency resolution of 1 Hz). The typical exposure time for a segment of observation is 3000 seconds so that M=3000 raw PDS are averaged together to create the PDS representative of the segment. Assuming that the algorithm finds a maximum excess of width 20 Hz (corresponding to a final rebinning factor NW of 20) at 5 σ, then N_{trial}=70 and the actual significance level of the signal is 99.998%. In the worst case of an excess of width 5 Hz (ie the minimum width considered) found at 3.5 σ (ie the minimum level obtained from the algorithm considered), N_{trial}=280 and the actual significance level is 92.7%. The low frequency PDS are scanned over a frequency range of 100 Hz. The exposure time of a raw PDS is $\sim$ 256 seconds (corresponding to a frequency resolution of 4×10^{-3} Hz). A PDS representative of a 3000 seconds segment is obtained from M=12 raw PDS. In the worst case of an excess of width 1 Hz (e.g NW=256) at 3.5 σ, then N_{trial}=100 and the true significance level is 97.0%.

3. Results

3.1. Light curves, color-color and hardness-intensity diagrams

Fig. 2 shows the global evolution of the persistent emission during our observations. Each point gives the 2-20 keV background

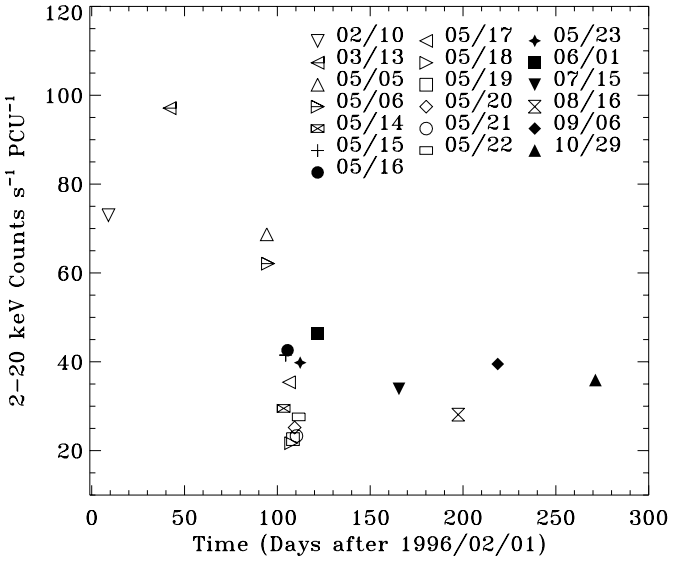

Fig. 2. Evolution of the persistent emission during the observations. The 2-20 keV background subtracted count rates are averaged over each observation. The corresponding exposure time is given in Table 2. The symbols labeled with the date of the observation will be used throughout the remainder of this paper.

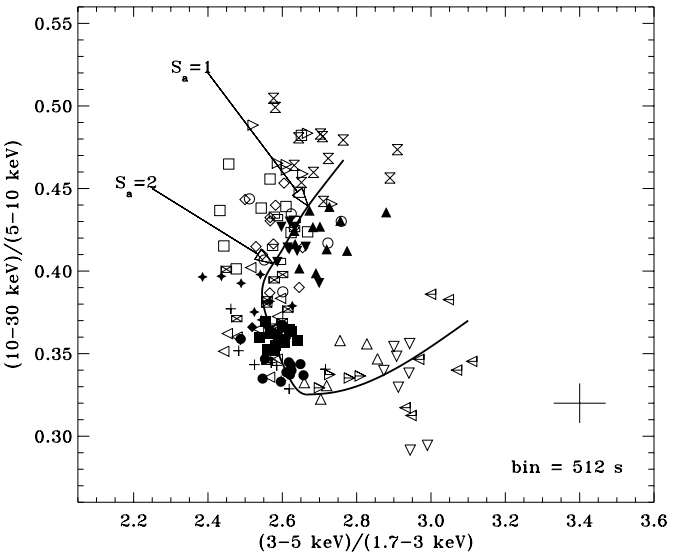

Fig. 3. Color-Color diagram. The binning time is 512 seconds and a typical error bar is shown. The thick line is the spline used to approximate the position on the color-color diagram. This position is quantified by the curvilinear coordinate S_a chosen arbitrary. The positions S_a=1 and S_a=2 are indicated by arrows.

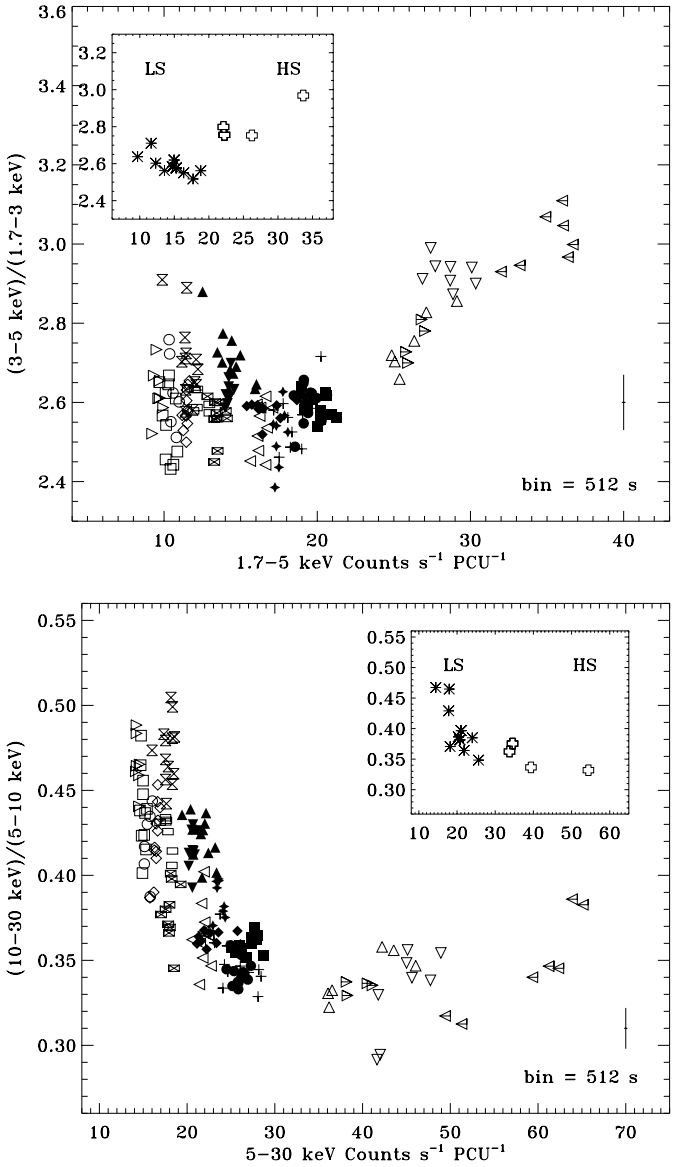

Fig. 4. Hardness-intensity diagrams for the soft color (top panel) and the hard color (bottom panel). In the main panels, the binning time is 512 seconds and a typical error bar is shown. In the inset panels, each point is the average over an observation. The asterisks and the large crosses indicate observations of the LS and HS respectively.

subtracted count rate integrated over a single observation. Each plotting symbol is associated with an observation (see the right corner of Fig. 2). As could have been anticipated from Fig. 1, our observations sampled various intensity states of the source: the PCA count rate changes by a factor of ~ 5 from roughly 20 to 100 cts s^{-1} PCU^{-1}. We also generated light curves in different energy bands between 2 and 30 keV for each observation. No substantial variation is noticeable in the persistent emission over timescales of a few hours.

Fig. 3 shows the color-color diagram. The points seem to form a "Banana" shape than can be approximated by a spline.

Fig. 4 shows the soft (top panel) and hard (bottom panel) colors as a function of the count rate. In the main panels, the binning time is 512 seconds while in the inset panels, each point is the average over an observation.

Looking at the behaviour of the source within an observation, we see, from the vertical tracks drawn by the points with a same symbol (main panels), that the colors can vary a lot while the intensity remains nearly constant, especially the hard color at low count rates.

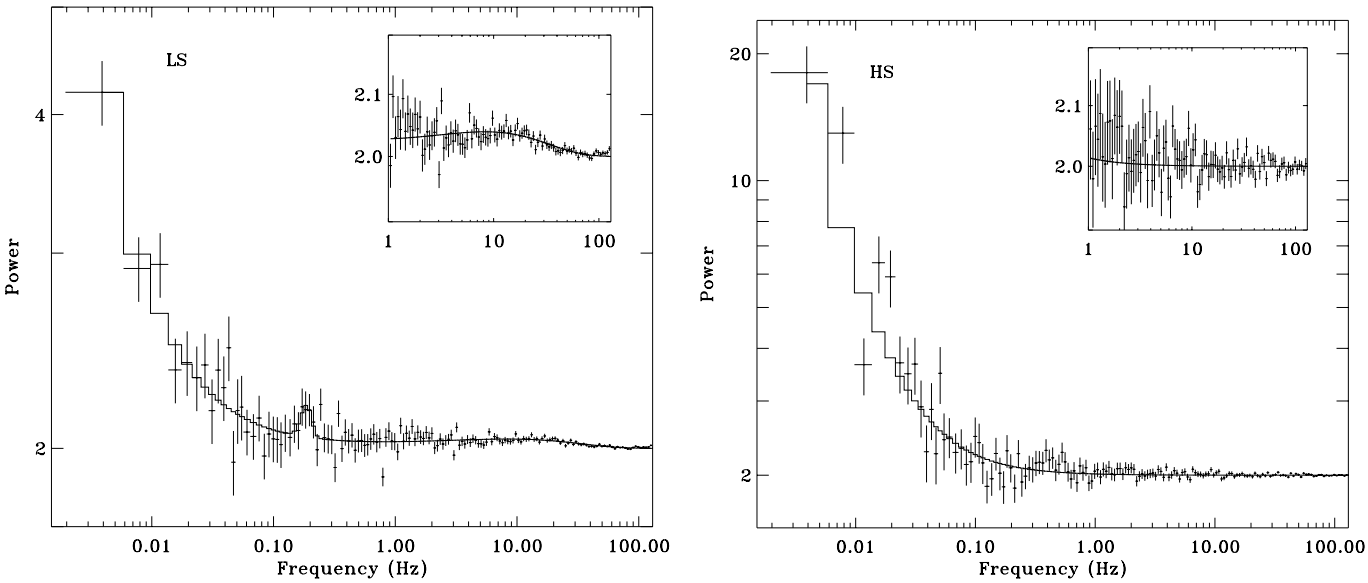

Fig. 5. Average PDS in the LS (left panel) and HS (right panel). The first one is obtained by averaging the PDS of the LS observations available in the 122 μs resolution mode: all the LS observations except a segment of the June 1st observation and the May 17th observation. The second PDS is obtained by averaging the PDS of the HS observations: February 10th, March 13th, May 5th and 6th (all obtained in 1 μs resolution mode). The total exposure time of the first PDS is more than 15 hours whereas it is only ~ 3 hours for the second one. The inset panel is a zoom of the PDS above 1 Hz. The solid lines are the best fits to the data.

Table 3. Best fit parameters obtained for the state averaged PDS shown in Fig. 5. The RMS is given in the frequency range $4 \times 10^{-3} - 1$ Hz for the VLFN, 1-128 Hz for the HFN and 0.1-0.3 Hz for the QPO.

State	Energy	VLFN		HFN			QPO			χ^2/d.o.f
		α	RMS	α	$\nu_{\rm cutoff}$	RMS	ν	FWHM	RMS	
	(keV)		(%)		(Hz)	(%)	(Hz)	(Hz)	(%)	
LS	5-30	$-1.03^{+0.16}_{-0.14}$	3.7±0.2	$0.5^{+0.2}_{-0.3}$	$18.9^{+6.4}_{-4.7}$	17.5±0.5	$0.19^{+0.03}_{-0.02}$	$0.02^{+0.04}_{-0.01}$	1.9±0.2	159/143
	2-30	-0.92±0.08	3.8±0.1	$0.6^{+0.2}_{-0.3}$	14±3	15.4±0.3	$0.19^{+0.02}_{-0.01}$	$0.014^{+0.032}_{-0.004}$	1.9±0.2	175/143
HS	5-30	$-1.24^{+0.14}_{-0.13}$	3.9±0.2	-	-	3.8±0.6	-	-	0.8±0.3	146/149

Looking at the global behaviour of the source along the observations (inset panels), two groups corresponding to two different spectral states may be distingished: we refer to the observations with the 5-30 keV intensity below and above ~ 30 cts s^{-1} PCU^{-1} as being in the low and high states (LS, HS) respectively. In the LS, we see a trend for the mean hard color to decrease as the intensity increases (Fig. 4 bottom), while the soft color remains nearly constant (Fig. 4 top), so that, on average, the emission softens with the intensity. On the contrary, in the HS, the hard color is nearly constant (Fig. 4 bottom), while the soft color increases with the intensity (Fig. 4 top), so that, on average, the emission hardens. 4U1915-05 is in a low intensity/hard spectrum regime in the LS and in a high intensity/soft spectrum regime in the HS. The spectral modeling of the persistent emission confirms this picture (Bloser et al. 2000). Assuming a source distance of 9.3 kpc, we derived a 2-20 keV luminosity of 1.4×10^{37} ergs s^{-1} on March 13th (when 4U1915-05 is the brighest and in the HS) and of 3.2×10^{36} ergs s^{-1} on May 18th (when 4U1915-05 is the faintest and in the LS).

3.2. Variability in the $4 \times 10^{-3} - 128$ Hz frequency range

3.2.1. Average power density spectra

In order to better characterize the source, we looked for possible correlations between the aperiodic variability and the spectral behaviour. We thus averaged together low frequency PDS of the LS on one hand (Fig. 5 left), and PDS of the HS on the other hand (Fig. 5 right), provided that they were obtained from the same timing mode data.

The average PDS of Fig. 5 (left) has an integrated RMS over the entire $\sim 4 \times 10^{-3} - 128$ Hz frequency range of 18.8 ± 0.6%. The PDS shows VLFN up to roughly 1 Hz and HFN around 20 Hz. The model C+PL+CPL provides a better fit than a simple PL (χ^2/d.o.f $\sim$ 166/146 and 324/149 respectively). Looking at Fig. 5 (right), we note an excess power around 0.2 Hz. We have fitted that excess with a Gaussian and assessed its significance through the standard F-test. We define P as the probability of rejecting the hypothesis that the fit is better with the additional Gaussian component. In the present case, we have P = 0.09, which means that the QPO is significant at a level of $\sim$ 91%.

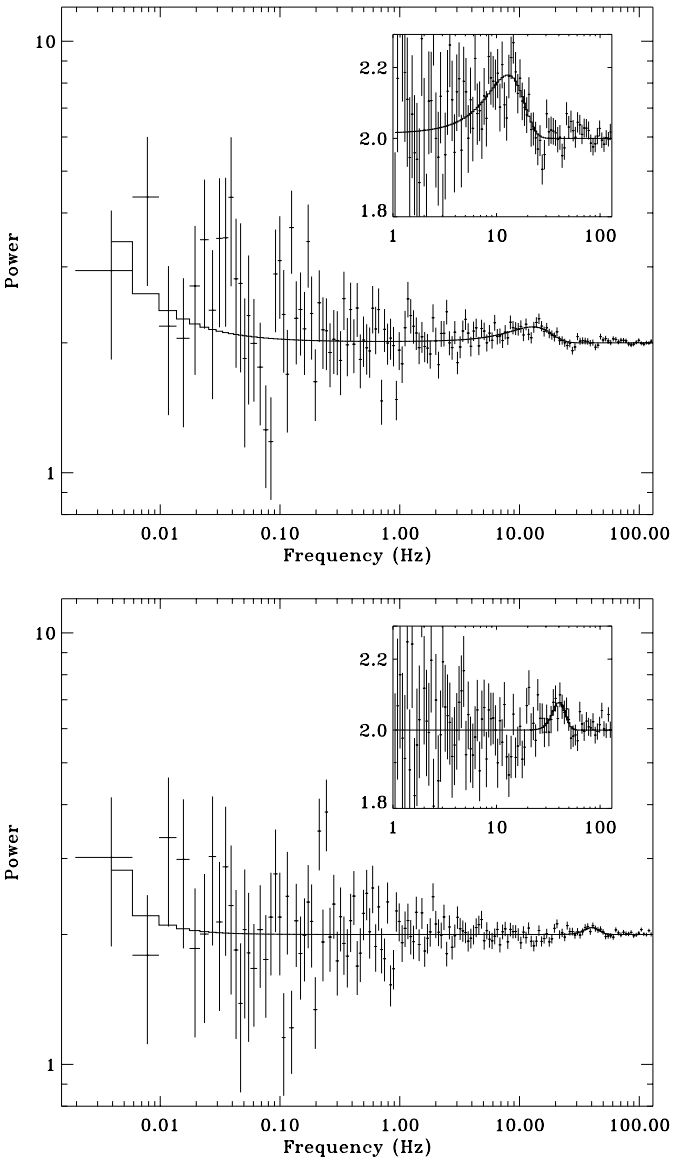

Fig. 6. PDS showing LFQPOs in the persistent emission of two segments of observations on October 29th (top panel) and June 1st (bottom panel). The mean count rate is 35 cts s^{-1} PCU^{-1} for the first PDS and 41 cts s^{-1} PCU^{-1} for the second (no background subtraction). The exposure time of both PDS is 1800 seconds. The inset panel is a zoom of the PDS above 1 Hz. The solid lines are the best fits to the data.

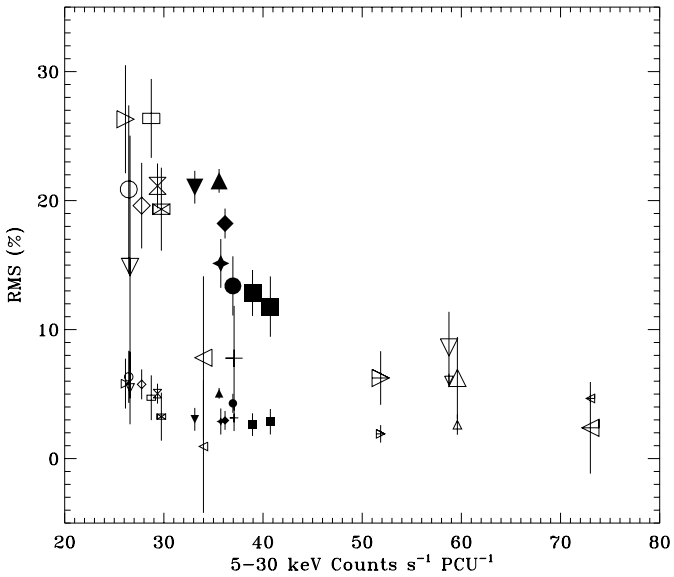

Fig. 7. RMS in the $4 \times 10^{-3} - 1$ Hz range (small symbols) and in the 1-128 Hz range (big symbols) versus count rate (no background subtraction).

With the 0.2 Hz Gaussian added, the results of the best fit are given in Table 3.

We have searched for the same signal in different energy ranges. As an example, in the 2-30 keV band, the significance of the 0.2 Hz signal reaches 93%. The best fit parameters are given in Table 3. In addition to the state averaged PDS, we computed PDS for each observing day. In some of these PDS, power excesses are visible around 0.2 Hz. However, they are statisticaly marginal with significance levels less than 90%.

In the HS, the source displays very low variability. The total RMS in the 5-30 keV energy range is 5.3 ± 0.2%. At low frequencies, the PDS is still dominated by VLFN up to roughly 0.1 Hz. But above this frequency, the PDS is consistent with having no power. No QPO nor HFN component are present in the PDS. The best fit parameters are given in Table 3.

Looking at each individual PDS, we found that what we called previously the HFN component in the state averaged PDS could be in fact resolved into broad QPO-like features of varying centroid frequencies. In the following, we call these features LFQPOs. Fig. 6 shows two examples of daily-averaged PDS where such a LFQPO is clearly detected. Detailed properties of the LFQPOs are given in the next section. To conclude, 4U1915-05 displays aperiodic variability below ~ 1 Hz (the VLFN) and quasi-periodic variability or no variability above 1 Hz.

Fig. 7 displays the RMS as a function of the count rate for each observation. The RMS is given in the $3 \times 10^{-3} - 1$ Hz frequency range where the VLFN dominates, and between 1-100 Hz where the LFQPO is detected. The RMS of the VLFN component ranges between ~ 3 and 6%, whereas the RMS above 1 Hz ranges between ~ 5 and 25%. In the LS, the RMS is high and decreases as the average count rate per observation increases. On the other hand, in the HS, the RMS, after reaching a low threshold, does not significantly vary as the count rate increases. Thus, the timing behaviour of 4U1915-05 is different in its two states.

3.2.2. Low frequency quasi-periodic oscillations

To further investigate the properties of the LFQPOs detected between a few Hz and 100 Hz in 4U1915-05 (see Fig. 6), and given their relative weakness in the persistent emission, we searched for them in the persistent and dipping emission combined rather than in the persistent emission alone. Although we note that we may be looking at different signals when combining the persistent and dipping emissions, we aimed to get the best signal

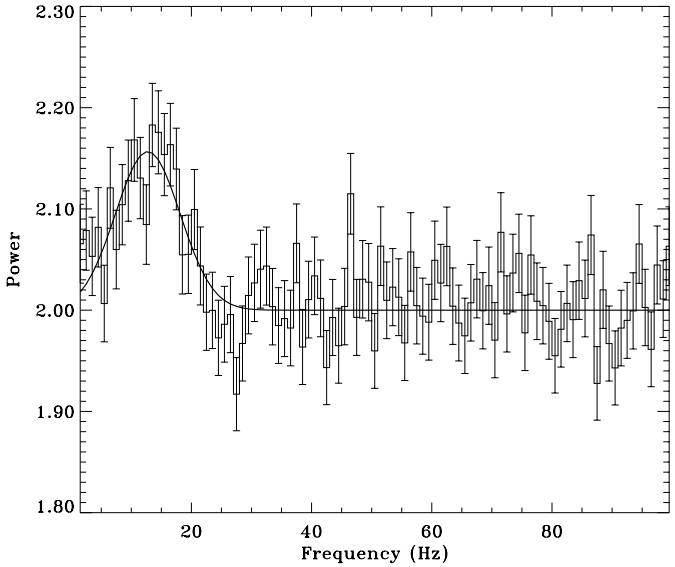

Fig. 8. PDS showing the LFQPO in a segment of the October 29th observation (persistent and dipping emissions combined). The solid line is the best fit of the QPO with a Gaussian.

to noise ratio. The study of the LFQPOs is carried out in the 5-30 keV energy range in order to make easier the comparison with the HFQPOs detected in that energy range with the best signal to noise ratio (see next section). The dipping is large but not complete in that energy range. So, adding the dipping parts, which represent roughly 40% of the data set, actually increases the signal to noise ratio. This is not negligible because 4U1915-05 is relatively faint in the PCA (2-20 keV background subracted count rate around 35 cts s^{-1} PCU^{-1}, to be compared with $\sim$ 30000 cts s^{-1} PCU^{-1} for Sco X-1) and observed with only 3 PCUs for more than the half of our observation (see Table 2). Furthermore, the ingress or egress of a dip lasts more than 1 second (typically 40 s). So, above 1 Hz where the LFQPOs are detected, the PDS of the persistent and dipping emission is not contaminated by the dip phenomenon itself. PDS were computed in the range $\sim 4 \times 10^{-3} - 128$ Hz the same way as for the persistent emission alone. We averaged together PDS of the same observation or the same segment.

The LFQPOs frequency, FWHM, RMS and significance level are listed in Table 4. Their frequency ranges between 5 and 80 Hz. Their FWHM is around 16 Hz but can vary from 0.5 to 45 Hz, so that their coherence (Q=ν/FWHM) changes roughly from 0.5 to 26 with a mean value of 4. The designation of QPO is then sometimes improper since this is usually used for signals with Q values greater than 2 (Van der Klis 1995). One of the LFQPOs is shown in Fig. 8. In the second segment of September 6th, we found an excess in the PDS between 1 and $\sim$ 50 Hz ($\sim 6.3\ \sigma$). A visual inspection of the PDS indicates that this excess is flat, yet above the noise level. For this reason, we were unable to fit it with a Gaussian, and therefore we do not consider this excess as a LFQPO, as defined above. Interestingly enough, however we note that the centroid of the excess ($\sim$ 30 Hz) would fall on the correlation between LFQPO frequency and the upper HFQPO frequency, as shown in Fig. 13 (see Sect. 4.4).

We looked for correlations between LFQPOs and spectral states. The bottom-left panel of Fig. 9 shows the LFQPO frequency versus the 5-30 keV count rate. All but one of the LFQPOs are detected in observations of the LS. For 4U1915-05, the LFQPO frequency seems to roughly correlate positively with the intensity, but the scatter is substantial.

The bottom-right panel of Fig. 9 shows the LFQPO RMS as a function of count rate. The RMS ranges from 5 to 20%. For the HS, we have derived upper limits ranging between 3 and 10% (see Table 4). No simple relation seems to connect the two quantities.

Recent works have shown that some timing features of similar systems were better correlated with the position on the color-color diagram than with the count rate (Méndez et al. 1999; Méndez & Van der Klis 1999). We thus examined the QPO properties as a function of the position on the color-color diagram.

Color-color diagrams are sensitive to changes of a few percent in flux ratios between energy bands. Observations allowed to show that during these subtle changes, the X-ray intensity was not a measure of the accretion rate since both positive and negative correlations between the two quantities could occur (Hasinger & Van der Klis 1989; Van der Klis 1994). The position on the color-color diagram is a better indicator of the spectral state and hence the accretion rate than the count rate.

The direction of evolution of the accretion rate on the color-color diagrams was inferred from X-ray luminosities and confirmed by multiwavelength and bursts observations (Hasinger et al. 1990; Van der Klis et al. 1990). In the atoll sources, the accretion rate is believed to increase from the island to the lower and then to upper banana states. For our analysis, we refer to the color-color diagram shown in Fig. 3. The spline shows the approximated track followed by 4U1915-05 during the observations. The direction of evolution of the accretion rate along the track is derived from the X-ray luminosity which globaly increases from the extremity located at the top of the diagram to the extremity located at the bottom (see Bloser et al. (2000) for details about spectral fitting).

Following Méndez et al. (1999), we called S_a the parametrization along this spline. S_a is a measure of the position of the source on the diagram. S_a was choosen to increase from top to bottom so that it is representative of the inferred evolution of the accretion rate. We determined the value of S_a for each segment of observation by projecting the corresponding point of the color-color diagram (inset panel of Fig. 3, where one point corresponds to one segment) on the spline. This value of S_a could then also be attributed to the LFQPO detected in the given segment. For LFQPOs detected in PDS averaged from several segments of the same observation day, we used the mean of the S_a values found for each segment. The bottom-left panel of Fig. 10 shows the LFQPO frequency as a function of S_a. A positive correlation is now clearly visible. In the bottom-right panel of Fig. 10, we show that the LFQPO RMS anticorrelates with S_a. In both plots, the scatter is now much smaller than in

Table 4. Properties of the QPOs detected above 3 σ (see text) in 4U1915-05 in the 5-30 keV energy range. We list the observation date (month/day) followed by the segment number or by an asterisk if all segments have been summed, the frequency, FWHM, RMS and significance of the LFQPOs (1-100 Hz) and HFQPOs (100-1400 Hz). The last column is the separation between the twin HFQPOs. All the values are inferred from Gaussians used to fit the QPOs. The reduced χ^2 are close to 1. The error bars are given for the 90% confidence level ($\Delta\chi^2$=2.7 for the variation of a single parameter). When no signal is present above our confidence threshold, we give a 3 σ upper limit on the RMS of a signal of FWHM 10 Hz for the LFQPOs and 50 Hz for the HFQPOs. The significances quoted here are for a single trial only. A more detailed assessment of the significance of the detections taking into account the number of trials may be found in the text (see Sect. 2.3.3). [a] flags detections at a significance level between 3 and 4 σ. The other signals have significance level greater than 4 σ. [b] The excess could not be fitted as a Gaussian (see text). Approximated values of the frequency, FWHM and RMS are given.

Obs	LFQPO				HFQPO				
	ν (Hz)	FWHM (Hz)	RMS (%)	σ	ν (Hz)	FWHM (Hz)	RMS (%)	σ	$\Delta\nu$ (Hz)
02/10 *			4				7		
03/13 *			3				6		
05/05 1	$72.3^{+6.5}_{-6.3}$ [a]	$22.1^{+12.7}_{-11.1}$	10.8±1.5	3.6			13		
05/05 2			9		$1263.9^{+1.8}_{-1.7}$ [a]	$6.8^{+3.8}_{-3.1}$	8.1±1.1	3.7	
05/06 1			10		$879.9^{+2.9}_{-2.7}$	$12.8^{+5.4}_{-5.2}$	9.9±1.1	4.5	
05/14 1			18		$946.7^{+16.1}_{-16.1}$	$77.2^{+28.8}_{-26.1}$	32.9±3.4	4.8	
05/14 2	$29.2^{+0.6}_{-0.6}$ [a]	$1.6^{+1.5}_{-1.0}$	8.3±1.4	3.0	$960.3^{+0.8}_{-0.9}$ [a]	$2.8^{+2.2}_{-1.5}$	10.2±1.5	3.4	
05/14 3			17		$839.5^{+26.0}_{-26.6}$ [a]	$93.9^{+46.5}_{-33.5}$	32.0±4.4	3.6	
05/15 1			13		$1055.3^{+17.1}_{-17.9}$	$80.4^{+35.8}_{-29.9}$	19.4±2.1	4.6	$348.4^{+28.1}_{-27.4}$
					$706.9^{+22.4}_{-20.9}$ [a]	$73.4^{+39.5}_{-36.5}$	16.4±2.4	3.4	
05/16 *	$31.1^{+13.6}_{-15.7}$ [a]	$45.2^{+29.0}_{-19.4}$	11.3±1.7	3.3	$1006.4^{+16.2}_{-16.6}$	$79.8^{+37.2}_{-29.9}$	16.4±1.7	4.8	$349.5^{+22.9}_{-24.7}$
					$656.9^{+16.2}_{-18.3}$ [a]	$53.7^{+32.5}_{-27.1}$	12.0±1.9	3.2	
05/17 *			8		$942.0^{+27.0}_{-26.1}$	$131.8^{+59.3}_{-44.3}$	21.7±2.2	4.9	
05/18 1			16		$577.2^{+32.3}_{-31.6}$	$146.5^{+64.6}_{-53.7}$	36.3±3.9	4.7	
05/18 2	$20.3^{+4.3}_{-4.6}$ [a]	$15.2^{+8.6}_{-6.8}$	18.6±2.7	3.4			23		
05/19 1	$19.1^{+2.8}_{-2.8}$	$12.2^{+7.1}_{-5.9}$	19.8±2.2	4.5			24		
05/20 *	$17.5^{+2.9}_{-3.3}$	$12.4^{+6.32}_{-5.0}$	13.8±1.6	4.3			20		
05/21 1	$8.0^{+0.4}_{-0.4}$	$2.0^{+0.7}_{-0.6}$	12.5±1.3	4.8			21		
05/21 2	$12.6^{+0.1}_{-0.1}$ [a]	$0.5^{+0.2}_{-0.2}$	8.1±1.1	3.7			25		
05/22 *	$14.0^{+3.2}_{-3.4}$	$18.6^{+9.4}_{-5.7}$	16.3±1.3	6.3			17		
05/23 1	$34.4^{+4.0}_{-3.0}$ [a]	$11.8^{+8.1}_{-4.7}$	8.5±1.1	3.9	$818.9^{+11.4}_{-10.9}$	$51.2^{+23.1}_{-18.4}$	13.9±1.5	4.6	
05/23 2	$31.8^{+2.2}_{-2.4}$	$12.6^{+6.3}_{-3.9}$	10.6±1.0	5.3	$845.5^{+15.9}_{-15.9}$	$78.4^{+36.2}_{-25.5}$	15.9±1.6	5.0	
06/01 1	$36.6^{+6.2}_{-7.0}$	$35.0^{+20.0}_{-12.2}$	12.1±1.0	6.0	$935.2^{+13.3}_{-13.3}$	$89.0^{+30.1}_{-25.2}$	16.6±1.2	6.9	
06/01 2	$35.2^{+0.7}_{-0.7}$ [a]	$2.2^{+1.5}_{-1.2}$	4.9±0.8	3.1	$911.3^{+16.8}_{-16.4}$	$103.2^{+43.8}_{-28.3}$	18.3±1.5	6.1	$352.9^{+17.3}_{-17.0}$
					$558.3^{+4.3}_{-4.6}$	$18.4^{+8.8}_{-6.9}$	9.8±1.2	4.1	
06/01 3			7		$953.1^{+13.9}_{-13.9}$	$71.7^{+24.8}_{-20.4}$	14.5±1.4	5.2	
07/15 *	$15.3^{+2.1}_{-2.3}$	$26.1^{+5.8}_{-4.8}$	15.4±0.6	12.8	$710.0^{+31.5}_{-30.7}$	$149.1^{+73.9}_{-48.7}$	17.8±1.4	6.4	
08/16 1	$12.6^{+2.2}_{-2.4}$	$11.3^{+5.0}_{-3.9}$	19.5±2.0	4.9	$513.6^{+0.2}_{-0.2}$	$1.2^{+0.6}_{-0.4}$	12.4±1.3	4.8	$290.0^{+4.7}_{-4.2}$
					$223.6^{+4.7}_{-4.2}$ [a]	$16.2^{+8.6}_{-5.9}$	18.3±2.5	3.7	
08/16 2	$11.8^{+1.4}_{-1.4}$	$11.7^{+3.8}_{-2.9}$	15.8±0.9	8.8	$538.1^{+15.3}_{-14.8}$ [a]	$55.4^{+27.1}_{-24.2}$	15.5±2.1	3.7	
08/16 3	$8.7^{+0.9}_{-1.0}$	$12.2^{+2.2}_{-1.9}$	19.6±0.7	14.0			15		
08/16 4	$12.9^{+1.2}_{-1.2}$	$6.9^{+3.7}_{-2.8}$	12.3±1.0	6.1			18		
09/06 1	$28.2^{+9.0}_{-9.9}$	$44.5^{+23.9}_{-16.1}$	15.3±1.5	5.1	$844.1^{+11.5}_{-10.8}$	$73.0^{+22.4}_{-19.5}$	20.2±1.5	6.7	
09/06 2	30 [b]	20	17	6.3	$808.4^{+9.5}_{-10.5}$	$39.6^{+21.8}_{-17.1}$	14.4±1.8	4.0	
09/06 3	$34.0^{+5.1}_{-5.2}$	$24.3^{+12.8}_{-8.9}$	12.5±1.3	4.8	$888.6^{+32.4}_{-30.2}$	$172.8^{+68.4}_{-66.7}$	22.5±2.0	5.6	
09/06 4	$45.7^{+2.8}_{-3.1}$ [a]	$10.0^{+6.3}_{-4.6}$	8.2±1.2	3.4	$923.8^{+23.2}_{-22.7}$	$125.4^{+56.6}_{-45.0}$	19.5±1.8	5.4	$340.5^{+24.2}_{-23.6}$
					$583.2^{+6.8}_{-6.5}$ [a]	$21.5^{+20.6}_{-10.8}$	9.7±1.4	3.5	
10/29 1	$12.9^{+0.7}_{-0.8}$	$10.2^{+1.5}_{-1.3}$	17.1±0.6	14.2	$610.9^{+24.4}_{-25.9}$ [a]	$88.4^{+48.9}_{-38.9}$	14.8±2.1	3.5	
10/29 2	$8.5^{+2.0}_{-2.0}$	$17.5^{+5.6}_{-3.8}$	16.4±0.8	10.2	$573.0^{+1.3}_{-1.4}$ [a]	$4.6^{+2.8}_{-2.3}$	7.6±1.1	3.5	
10/29 3	$20.6^{+2.7}_{-2.8}$	$25.0^{+7.9}_{-6.3}$	16.8±0.8	10.5	$610.2^{+4.1}_{-4.2}$	$20.7^{+8.5}_{-6.4}$	11.9±1.2	5.0	

the previous plots where the count rate was involved. Note that we have also studied the evolution of the LFQPOs as a function of the hard color (10-30 keV/5-10 keV). We concluded that the hard color was a worse indicator of the timing behaviour than S_a: the evolution of the soft color had to be taken into account.

3.3. Discovery of high frequency quasi-periodic oscillations

Now, we report on the discovery of HFQPOs from 4U1915-05. The analysis has been carried out in the 5 to 30 keV energy range because in other sources, it is known that HFQPOs are

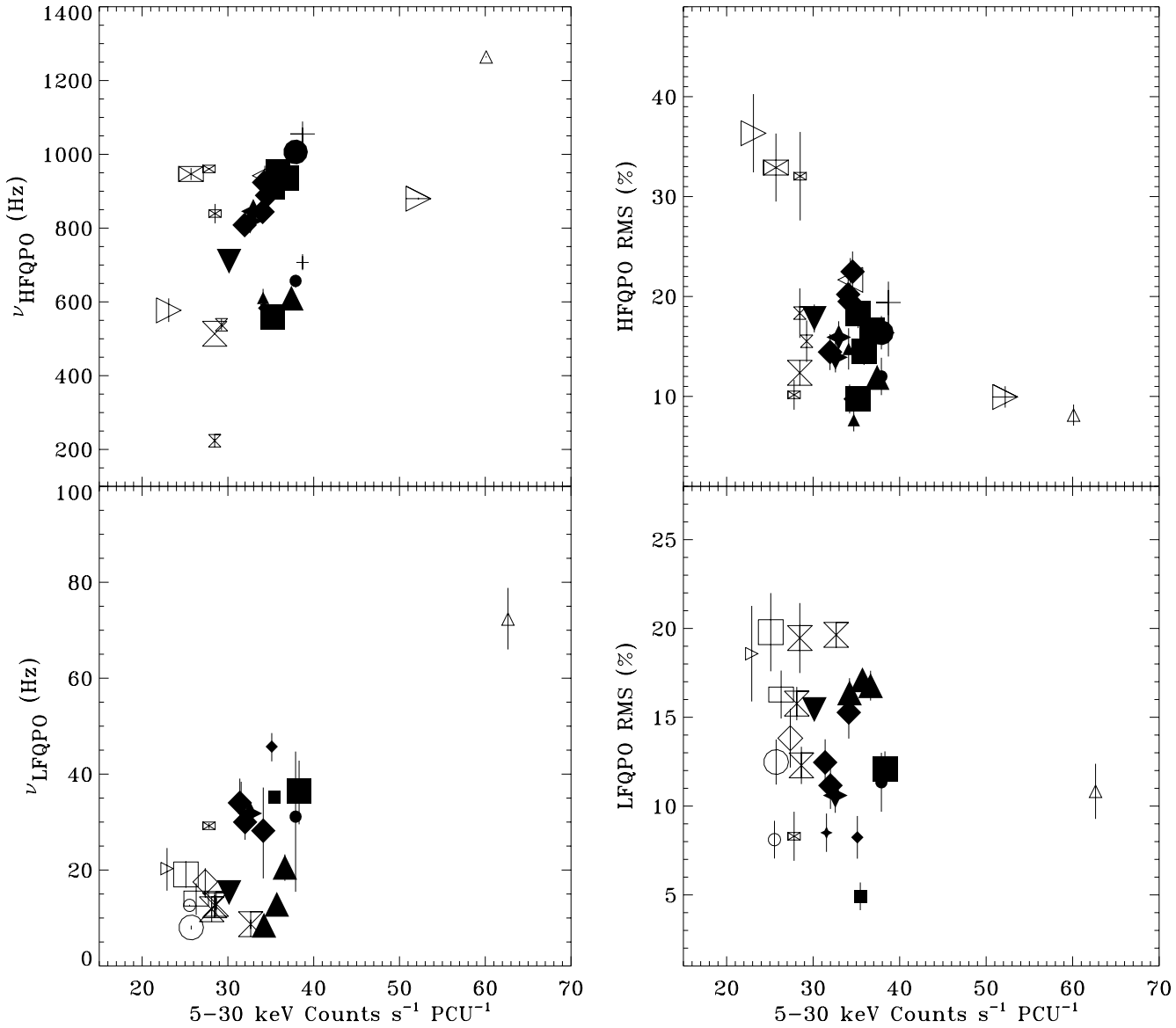

Fig. 9. Left: LFQPO (bottom panel) and HFQPO (top panel) frequency as a function of the 5-30 keV count rate (no background subtraction). Right: LFQPO (bottom panel) and HFQPO (top panel) RMS as a function of the 5-30 keV count rate. Small symbols are used for detections between 3 and 4 σ, big symbols for detections above 4 σ.

more easily detected in this energy band, as in, e.g. KS1731-260 (Wijnands & Van der Klis 1997). The persistent and dipping emission were combined to increase the signal to noise ratio (see Sect. 3.2.2).

The results are reported in Table 4 (either the observations or the segments). The HFQPOs frequency ranges between ~ 200 and 1300 Hz. Their FWHM is around 70 Hz and coherence around 50. Their RMS amplitude is high ($\sim 17\%$). One of the strongest HFQPO signals is shown in Fig. 11.

We detect twin HFQPOs in 5 segments or observations (Table 4). For four of them, the frequency separation is consistent with being constant. The mean separation is 348 ± 12 Hz. For the fifth, the separation is 290 ± 5 Hz, thus inconsistent with the previous value. We note that this pair of QPOs occur at 514 and 224 Hz whereas the four other twin peaks occur above 550 Hz. The twin HFQPOs detected in a segment of the June 1st observation are shown in Fig. 12.

HFQPOs were not detected in observations with the largest count rates (February 2nd, March 13rd) with upper limits of $\sim 6\%$ on the RMS (Table 4). HFQPOs were not detected either in the lowest count rate regime (May 18th to May 22nd); this might be due to a lack of sensitivity. Indeed, only 3 PCUs were working during these observations (see Table 2) and the upper limits on the RMS are not constraining ($\sim 20\%$, see Table 4).

The top-left panel of Fig. 9 shows the HFQPO frequency as a function of count rate. In this diagram, we observe a branch between 700 and 1100 Hz where the frequency strictly correlates with the count rate. A second parallel branch seems to be drawn at lower frequencies. However, some of the HFQPOs of that branch do not have a simultaneous twin peak in the upper branch.

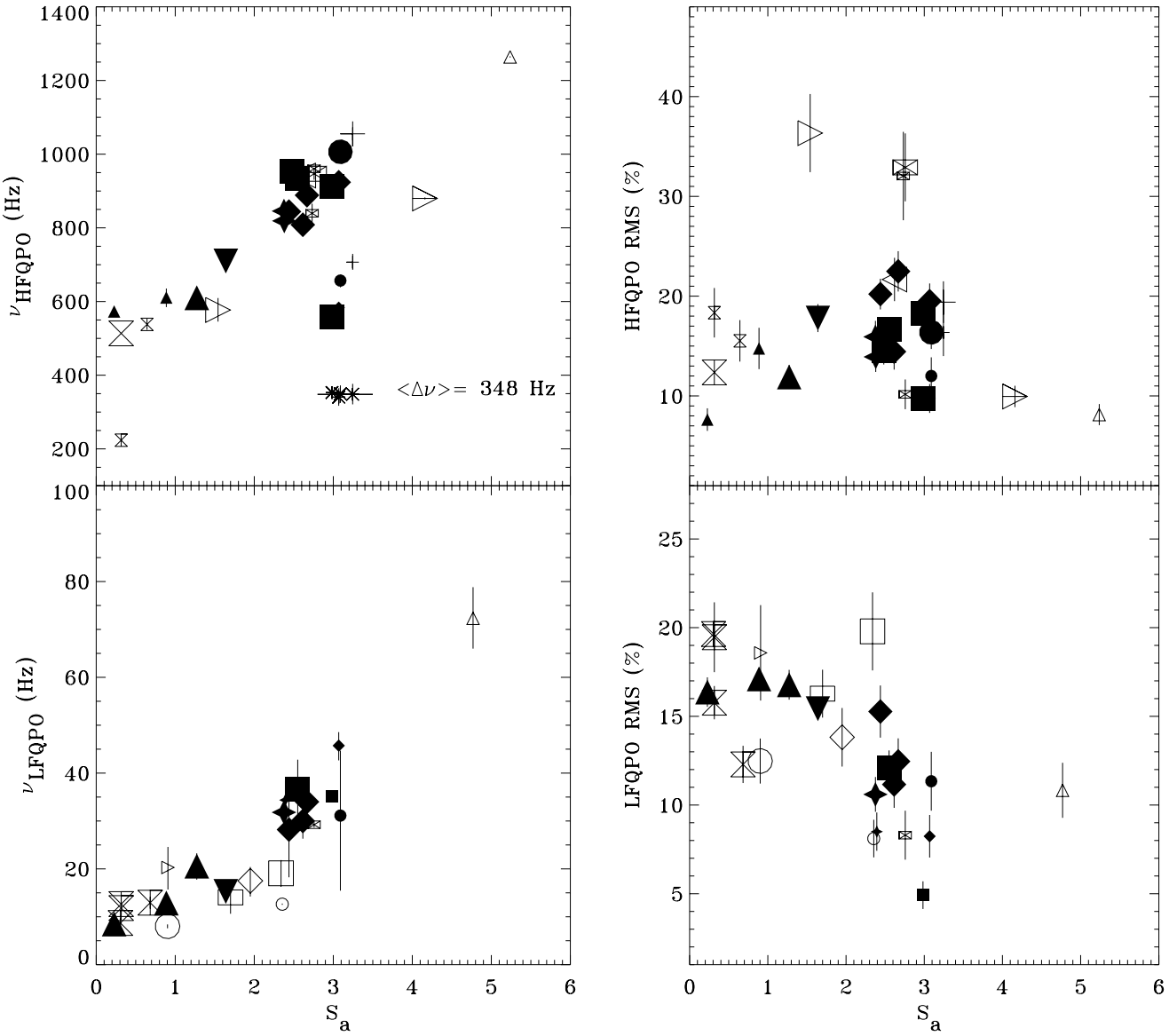

Fig. 10. Left: LFQPO (bottom panel) and HFQPO (top panel) frequency as a function of the position S_a on the color-color diagram. The asterisks represent the frequency separation of the twin HFQPOs. The solid line is the average separation. Right: LFQPO (bottom panel) and HFQPO (top panel) RMS versus S_a. Small symbols are used for detections between 3 and 4 σ, big symbols for detections above 4 σ.

In the lowest count rate regime, the frequency does not follow anymore a simple relation with the count rate.

The top-left panel of Fig. 10 shows the HFQPO frequency as a function of S_a. The frequency versus S_a relation appears much simpler than the frequency versus count rate relation. We can now easily identify the upper and lower HFQPOs. The frequency of the upper HFQPO is now well correlated with S_a within its full range. The four twin peaks above 550 Hz are detected within a narrow range of S_a around 3. Their frequency separation is shown with an asterisk on Fig. 10. The pair of QPOs at 224 Hz and 514 Hz appears at the lowest S_a and hence lowest inferred accretion rate. Concerning the HFQPO RMS, we show that, surprisingly, it is better correlated (negatively) with the count rate than with S_a (top-right panel of Fig. 9 and 10 respectively).

3.4. Correlation between low and high frequency quasi-periodic oscillations

Fig. 10 (left panel) shows the parallelism between HF and LF QPOs. Their frequency increases similarly with S_a. In Fig. 13, we show the relation between LFQPO and upper HFQPO frequencies when both QPOs are detected simultaneously and above 4 σ. The correlation between the two frequencies is obvious. It can be approximated with a power law of the form $\nu_{LFQPO} = \alpha\nu^{\beta}_{HFQPO}$. The first attempt of fitting the data provided a high reduced χ^2 because of the point representing the July 15th observation lying off from the fit. We thus made the fit taking out this point. We obtained $\alpha = (6 \pm 10) \times 10^{-4}$ and $\beta = 1.6 \pm 0.3$ (reduced χ^2 of 1.1) as parameters of the power law drawn as the solid line on Fig. 13.

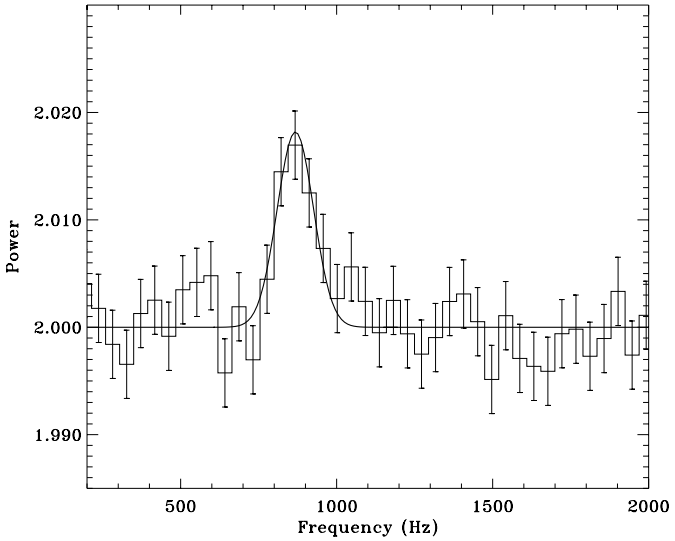

Fig. 11. PDS for the September 6th observation. The HFQPO is fitted with a Gaussian.

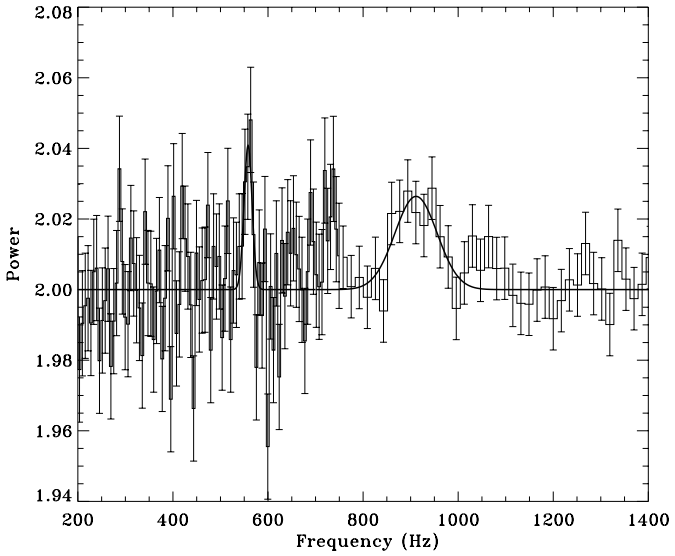

Fig. 12. The twin HFQPOs fitted with Gaussians detected in a segment of the June 1st observation. For display purposes, two different frequency binnings have been used.

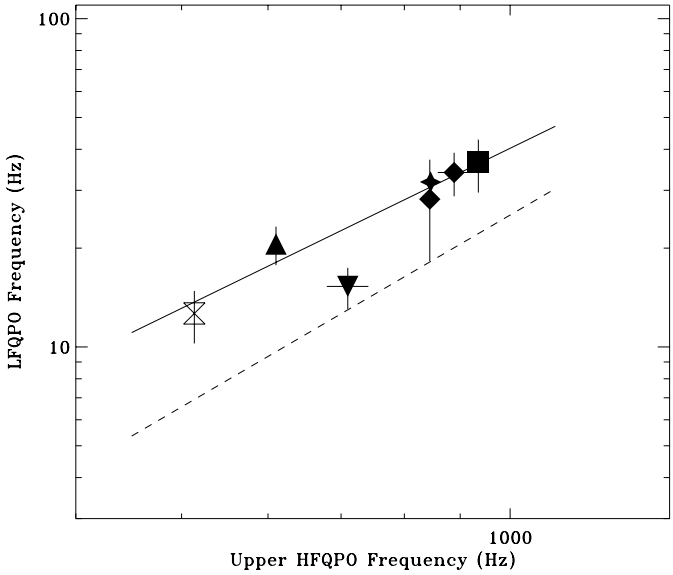

Fig. 13. LFQPO frequency as a function of the upper HFQPO frequency. We report signals detected simultaneously above 4 σ. The solid line is the powerlaw of index 1.6 fitting the data. The dashed line is the precession frequency (Lense-Thirring and classical contributions (Stella & Vietri 1998)) assuming standard parameters for the neutron star (see text) and a spin frequency of 348 Hz.

3.5. Search for oscillations in bursts

For the bursts recorded in the 122 μs resolution mode, we have computed thirty PDS of 1 second duration so that they covered the rising and decaying parts of the bursts. Each was individually searched for excess power. No such excesses were found either in individual PDS nor in their sum. We therefore conclude that no QPOs were found in those bursts. We have set upper limits on the RMS, assuming a 3 σ signal of FWHM 1 Hz in the PDS. We derive a 3 σ upper limit of 3.2% for the October 29th burst, and of 2.8% for the August 16th burst.

For the burst catcher mode, the situation is slightly different. The data cover only the first 3.75 seconds of the bursts, and the Nyquist frequency is 256 Hz which is below the typical frequency of a burst oscillation (Van der Klis 1999). Note however that coherent oscillations were found at 7.6 Hz in a burst from Aql X-1 (Schoelkopf & Kelley 1991). For the burst that occured on May 5th, no significant signals were found in PDS computed for different segments durations (ranging from 1.25 to 3.75 seconds). We have derived a 3 σ upper limit of 2.8% (FWHM=1 Hz) for the 3.75 seconds burst duration.

For the June 1st burst, we have also computed an FFT from the 3.75 seconds data set. When the PDS so computed is rebinned by a factor of 4 ($\Delta\nu = 1.1$ Hz), two signals are detected by our algorithm; 117.5 Hz (5.4 σ, RMS=3.5 ± 0.4%), 225.7 Hz (5.0 σ, RMS=2.8 ± 0.2%). However, in the case of these PDS, the corresponding significance detection level (taking into account the number of trials; see Sect. 2.3.3) is only 85%, which is insufficient to claim a detection.

4. Discussion

4.1. The nature of 4U1915-05

The classification introduced by Hasinger and Van der Klis (1989) distinguishes two classes of LMXBs, the Z and the atoll sources. We list the main evidence suggesting that 4U1915-05 is an atoll source. First, 4U1915-05 has always been detected at X-ray luminosities below $\sim 1.5 \times 10^{37}$ ergs s^{-1}, which is typical for atoll sources. The Z sources are roughly 10 times brighter. Second, the orbital period of 4U1915-05 (50 min) is among the shortest observed for LMXBs. Now, it is observed that Z sources have longer periods (more than 10 h) than atoll sources, consistent with the idea that their companions are giants or subgiants (Van der Klis 1995). Furthermore, almost all

persistent dippers and bursters belong to the atoll class (Cyg X-2 and GX 17+2 are the only Z sources to display type I bursts (Kahn & Grindlay 1984; Smale 1998; Sztajno et al. 1986)). Finally, no Z track in the color-color diagram has been observed neither in the GINGA data (Yoshida 1992), nor in the RXTE data. Hence, this favors the idea that 4U1915-05 belongs to the atoll class, as suggested by Yoshida (1992).

4.2. The states of 4U1915-05

Identifying the different atoll states in 4U1915-05 is not straightforward. From the hardness-intensity diagrams, we can see that the emission, on average, varies along the observations from a HS to a LS that could correspond to banana and island states respectively. However, we do not observe clearly separated regions in the color-color diagram but rather a continuous banana shape. Furthermore, in its LS, 4U1915-05 does not display HFN which is the typical aperiodic variability of atoll sources in their island state; 4U1915-05 displays VLFN in its both states. This behaviour was observed in the GINGA data as well. Unlike Yoshida (1992) who associated the two regimes with island and banana states, we believe that, during our observations, the source was not in its island state; it probably remained on the banana branch and hence never reached the state which may be at even lower luminosity. Such a state may have been observed by BeppoSAX (Church et al. 1998) since extrapolating the spectral parameters reported by Church et al. (1998) into the 2-50 keV energy range gives a luminosity of 4.5×10^{36} ergs s^{-1} while the luminosity derived from the RXTE observations in the same energy band ranges between 5×10^{36} and 1.4×10^{37} ergs s^{-1} (Bloser et al. 2000).

The properties and presence of HFQPOs strongly depend on source states. For atoll sources, HFQPOs seem to occur at intermediate inferred accretion rates: they are generally not observed in extreme island or upper banana states corresponding respectively to the lowest and highest accretion rates in a given source, as in e.g. 4U1608-52 (Méndez et al. 1999). Twin simultaneous HFQPOs have now been detected in all atoll sources showing kHz variability but Aql X-1 (Van der Klis 1999). They are always seen during banana states with the exception of 4U1728-34 (Ford & Van der Klis 1998; Strohmayer et al. 1996; Méndez & Van der Klis 1999) and 4U1735-44 (Ford et al. 1998b). This gives further support to the idea that 4U1915-05 was in a banana state during our observation. The highest intensity state where no HFQPO is detected (February and March observations) was therefore more likely the upper banana state. The lowest intensity state was likely the lower banana state, although no HFQPO is detected during May 18th to 22nd observations where the count rate is the lowest; maybe due to a lack of sensitivity (the RMS upper limits corresponding to these observations and quoted in Table 4 are not really constraining).

4.3. Tracking the accretion rate with S_a

It has been shown that the relation between HFQPO frequency and intensity could be much more complex than a roughly one to one correlation as for example in 4U1820-30 (Smale et al. 1997). Numerous branches are clearly visible in the HFQPO frequency versus intensity diagram made with an extensive set of data from 4U1608-52 and 4U1728-34 (Méndez et al. 1999; Méndez & Van der Klis 1999). Zhang et al. (1998) also showed that Aql X-1, observed in very distinct flux or count rate ranges, could display HFQPOs in the same frequency range. The absence of a simple correlation had previously been noticed in 4U1705-44 (Ford et al. 1998a). For 4U1608-52, the HFQPO frequency was reported to correlate well with the count rate but only on timescales of hours (Méndez et al. 1999). Thus, the relation between HFQPO frequency and intensity seems to differ from source to source; sometimes being complex. On the contrary, the position on color-color diagram yields a more universal and unique relation as in, e.g. 4U1608-52, 4U1728-34 (Méndez et al. 1999; Méndez & Van der Klis 1999). Our study of 4U1915-05 confirms these results. The HFQPO frequency has a simpler relation with the position S_a on the color-color than with the count rate (Fig. 9 and 10). The frequency is well correlated with S_a within its full range.

Now, currently admitted models for HFQPOs, which are beat frequency models (BFM), involve a bright spot at a specified radius of the Keplerian disk, e.g. the sonic radius in the "sonic-point model" (Miller et al. 1998c) to produce the upper HFQPOs. As the accretion rate increases, the disk inner radius moves inwards until the innermost stable orbit is reached. Then, the HFQPO frequency is supposed to correlate with the accretion rate up to a saturation. Thus, the observed complex relations between HFQPO frequency and count rate show that the count rate is not as good as S_a to track the accretion rate. This confirms the studies carried out with EXOSAT data which revealed the position on color-color diagrams as a better indicator of accretion rate than intensity (Hasinger & Van der Klis 1989; Van der Klis et al. 1990; Hasinger et al. 1990).

However, the position on the color-color diagram may not be the only or the best indicator of the accretion rate or (and) of the timing behaviour. The properties of the HFQPO RMS amplitude found in 4U1915-05 (Fig. 9 and 10) may be new evidence for this. Indeed, in the sonic-point model, the HFQPO amplitude is expected to decrease as the accretion rate increases: the optical depth and electron density increase near the neutron star, and the oscillations generated there are more attenuated during their propagation (Miller et al. 1998c). Therefore, one would expect the HFQPO RMS to be anticorrelated with the accretion rate. However, for 4U1915-05, the HFQPOs RMS does not seem to be anticorrelated with S_a but rather may be anticorrelated with the count rate (Fig. 10 and 9). Thus, the timing properties do not probably depend only on the position S_a. Furthermore, it is not clear why the HFQPOs RMS amplitude and frequency would be driven by different parameters.

Moreover, we have shown that 4U1915-05 can display different timing behaviours (presence or absence of HFQPOs) during observations overlapping in the color-color diagram. The same situation occurs in other sources, e.g. 4U1636-53 (Méndez 1998).

One explanation may be that these timing behaviours are in fact the same but seem different in appearance because of instrumental limitations. For example, a QPO may be present in two observations overlapping in the color-color diagram but not detected in one of them because one of the detectors has been switched off leading to a loss of sensitivity (see e.g. the RMS upper limits in Table 4).

A second explanation may be that within the timespan for which S_a is computed, the source might have moved in and out the S_a span, washing out temporal signals.

Another explanation is that the source has actually intrinsically different timing behaviours. In this case, this is evidence that the position in the color-color diagram is not the best indicator of the timing behaviour of a source. Then two different conclusions may be considered. First, assuming that the timing behaviour is governed by the accretion rate, then S_a is not a good indicator of the accretion rate. This quantity may be better represented by a combination of parameters or by other parameters than S_a. Second, assuming that S_a is a good indicator of the accretion rate, then the timing behaviour is not governed only by the accretion rate.

4.4. Low and high frequency quasi-periodic oscillations

LFQPOs between a few and $\sim$ 80 Hz have now been observed in several atoll sources (see Table 1). In 4U0614+09 (Ford 1997), 4U1608-52 (Yu et al. 1997), 4U1702-43 (Markwardt et al. 1999), 4U1728-34 (Strohmayer et al. 1996; Ford & Van der Klis 1998), KS1731-260 (Wijnands & Van der Klis 1997) and 4U1735-444 (Wijnands et al. 1998c), such LFQPOs are detected simultaneously with HFQPOs. In the case of 4U0614+09, 4U1728-34 and 4U1702-43, the LFQPO frequency is observed to increase with the HFQPO frequency and with the intensity of the source. First, this indicates that the LFQPOs detected in atoll sources are comparable to the horizontal branch QPOs (HBOs) detected in Z sources, suggesting that similar physical processes are at work in both kind of LMXBs. Second, this indicates that LF and HFQPOs are produced either by related mechanisms or by the same mechanism seen under different aspects or occuring at different locations in the disk. Our study of 4U1915-05 confirms both these conclusions. For the first time, we show a LFQPO in an atoll source varying in frequency and RMS amplitude as a function of the position on the color-color diagram (Fig. 10) the same way as HBOs in Z sources. We note however that in 4U1915-05, the LFQPOs are not strictly correlated with the source intensity, which is a characteristic of HBOs and also of the atoll sources mentioned above showing LFQPOs and HFQPOs. 4U1915-05's behaviour is thus different in this respect. This may be explained by the fact that in 4U1915-05, the intensity is not correlated with the position in the color-color diagram over the entire range where LFQPOs are detected. On the contrary, the intensity is strictly correlated with the position in the color-color diagram in horizontal branches (Van der Klis 1995) and probably in some portions of the track of atoll sources. In 4U1915-05, we clearly show (Fig. 10 and 9) that S_a, and not the count rate, is the key parameter of the quasi-periodic variability at low frequencies. Thus, the HF and LFQPOs frequencies depend the same way upon S_a.

Psaltis et al. (1999a) have shown that the frequency of the QPOs detected between 0.1 and 100 Hz in numerous Z, atoll or black hole binaries, simultaneously with HFQPOs followed one of a small number of correlations with the lower HFQPO frequency. For 4U1915-05, we could detect simultaneously the LFQPO and the lower HFQPO only during three segments. On the diagram derived by Psaltis et al. (Psaltis et al. 1999a, see their Fig. 2), these points would fall in the region where the two main correlations merge. Hence, our RXTE observation does not help to conclude about the unified picture suggested for QPOs.

The fact that HBOs and HFQPOs have now been observed simultaneously in Z sources, as in Cyg X-2 (Wijnands et al. 1998a) calls into question the models proposed for QPOs. Indeed, the magnetospheric BFM was first proposed to explain the HBOs in Z sources (Alpar & Shaham 1985). Later, the same model was suggested to explain the HFQPOs (Strohmayer et al. 1996) observed both in atoll and Z sources. But simultaneous LFQPOs and HFQPOs are difficult to explain with the same model. This requires that the disk is still present inside the radius where the magnetosphere couples the disk and channels the matter (Miller et al. 1998c). In this case, HBOs and HFQPOs can be explained both with the magnetospheric BFM. Psaltis et al. (1999b) have shown that the correlations observed between HBO and HFQPO frequencies in Z sources were indeed consistent with this model. However, this result has been shown so far for Z sources only. The striking similarities between the LFQPOs detected in 4U1915-05 and HBOs suggest that both phenomena could be interpreted within a same model. But the magnetospheric BFM may not be easily extrapolated to atoll sources because of their lower inferred magnetic fields and accretion rates.

Another possible interpretation comes from Stella and Vietri (1998) who proposed that the LFQPOs observed around 15-50 Hz in several atoll and Z (horizontal branch) sources could result from the precession of the innermost disk regions. In the first version of this model, the LFQPO frequency is the nodal precession (ν_{nod}) of slightly titled orbits in these regions. This precession frequency (relativistic -Lense-Thirring- and classical contributions) depends on the equation of state of the neutron star but also on its spin frequency and on the Keplerian frequency of the innermost accretion disk region. In the framework of BFMs, these latter frequencies are inferred for LMXBs displaying twin HFQPOs, from the frequency separation of the peaks and the frequency of the upper peak respectively. The precession frequency is predicted to vary approximately as the square of the innermost Keplerian frequency. For 4U1915-05,

the LFQPO frequency varies as $\nu_K^{1.6}$ where ν_K is the inferred Keplerian frequency (see Fig. 13). This is not far from the expected quadratic dependence within the errors. However, the observed LFQPO frequency is ~ 2 times greater than the expected precession frequency drawn as a dashed line on Fig. 13. We assumed a neutron star spin frequency of 348 Hz which is the mean peak separation between the twin HFQPOs detected in 4U1915-05. Furthermore, we used the same parameters as Stella and Vietri (1998) for the neutron star: mass $M = 1.97\mathrm{M}_\odot$, ratio $I_{45}/M = 1.98$ where I_{45} is the moment of inertia in units of 10^{45} g cm^2. With these values, Stella and Vietri (1998) found that the precession frequency matched the LFQPO frequency for three different atoll sources (4U1728-34, 4U0614-09 and KS1731-260). Since the neutron star parameters used yield precession frequencies close to the maximum values that can be reached keeping the parameters in the ranges allowed in classical neutron star models, it is unlikely that the Lense-Thiring model can be pushed up to match the LFQPOs in 4U1915-05. The precession frequencies are actually lower than the observed LFQPOs frequencies for any values of M and I_{45}/M within their reasonable respective ranges. This would also be the case if the spin frequency were lower than the one inferred from the twin peaks separation (348 Hz). On the opposite, the precession frequencies would roughly match the LFQPOs if the spin frequency were twice that value ($\sim$ 700 Hz). With a spin frequency of 348 Hz, matching the observed LFQPO frequencies with precession frequencies would require a ratio I_{45}/M of $\sim$ 3.5 which is too large. Indeed, this ratio is inferred to be in the range $\sim$ 0.5-2 for realistic rotating neutron star models (Stella & Vietri 1998; Marković & Lamb 1998; Kalogera & Psaltis 2000; Miller et al. 1998a).

Similar conclusions have been reached for 4U1728-34 (Ford & Van der Klis 1998, from a larger set of data than the one used by Stella and Vietri (1998), 4U1735-44 (Wijnands et al. 1998c), 4U1702-42 (Markwardt et al. 1999, in this case, the required ratio I_{45}/M is only 2.3 which is closer of the accepted range than for other sources) and for the Z sources GX 17+2, GX 5-1, GX 340+0, Cyg X-2 and Sco X-1 (Stella & Vietri 1998; Jonker et al. 1998; Psaltis et al. 1999b; Kalogera & Psaltis 2000). For the atoll source 4U1608-52, the precession frequency model does not seem to apply either: the spin frequency predicted from the Lense-Thirring model (Yu et al. 1997) is inconsistent with the one inferred from the frequency separation of the twin HFQPOs later observed (Méndez et al. 1998b,c). In summary, the LFQPOs roughly follow the dependence upon the Keplerian frequency expected within the Lense-Thirring model but occur at a frequency lower than the precession frequency for a growing group of binaries that now includes 4U1915-05. Thus, in order to explain the LFQPOs with the Lense-Thirring effect, further hypothesis are required (Marković & Lamb 1998; Morsink & Stella 1999; Armitage & Natarajan 1999; Kalogera & Psaltis 2000; Schaab & Weigel 1999). Another possibility is that the LFQPOs correspond to the second harmonics of the precession frequency $2\nu_{nod}$ instead of ν_{nod} as proposed in a second version of the Lense-Thirring model, maybe because of a modulation at twice the precession frequency generated at the two points where the inclined orbit of the blobs intersects the disk (Vietri & Stella 1998; Morsink & Stella 1999; Stella & Vietri 1998; Stella et al. 1999).

However, Psaltis et al. (1999b) and Schaab and Weigel (1999) noticed another discrepancy with the model: the LFQPO frequency does not follow the expected quadratic dependence on the Keplerian frequency when the latter frequency is greater than 850 Hz in Z sources. In addition, radiation forces in the disk could significantly affect the precession frequencies and thus possibly challenge the Lense-Thirring model as the explanation for the LFQPOs (Miller 1999). Thus, the LFQPOs origins and relations with HFQPOs remain unclear.

Another model proposes to interpret both the LF and HF QPOs within the same framework: the two-oscillator model (Osherovich & Titarchuk 1999b; Titarchuk & Osherovich 1999; Titarchuk et al. 1999). In this model, the lower kHz QPO is the Keplerian frequency ($\nu_K \sim 700$ Hz) at the outer edge of the boundary layer between the Keplerian disk and the neutron star. Blobs thrown out from this region into the magetosphere oscillate in both radial and perpendicular modes to produce an upper kHz QPO (at $\nu_h \sim 1000$ Hz) and a low frequency QPO (at $\nu_L \sim 50$ Hz) respectively. Furthermore, viscous and diffusive processes within the boundary layer produce respectively a low frequency QPO (at $\nu_V \sim 30$ Hz) and a break (at $\nu_b \sim 8$ Hz) in the PDS. In this model, the angle δ between the rotational frequency $\nu = \Omega/2\pi$ of the magnetosphere and the normal to the neutron star disk is not zero.

The various observed QPOs of Sco X-1, 4U1728-34 and 4U1702-42 have been succesfully identified in the framework of the two-oscillator model (Titarchuk et al. 1999; Osherovich & Titarchuk 1999a). The angle δ derived is $8.3^\circ \pm 1.0^\circ$, $5.5^\circ \pm 0.5^\circ$ and $3.9^\circ \pm 0.2^\circ$ respectively for each source. Furthermore, the predicted variation of ν_b as $\nu_V^{1.6}$ has been checked for number of atoll and Z sources (Titarchuk et al. 1999).

For 4U1915-05, the identification of the observed QPOs is not straightforward. 4U1915-05 does not show any break in its PDS. Only one LFQPO is detected in the frequency range where QPOs are predicted to be present at ν_V, ν_L and $2\nu_L$.

We tried however to test the two-oscillator model. Ω, ν_K and ν_h follow the relation $\nu_h^2 = \nu_K^2 + (\Omega/\pi)^2$ (see e.g., Eq. 2 in Osherovich and Titarchuk (1999a)), so that the rotational frequency can be derived when twin HFQPOs are detected simultaneously and interpreted as ν_K and ν_h.

The bottom panel of Fig. 14 shows the inferred rotational frequency as a function of the lower HFQPO frequency, for the four segments where twin HFQPOs are detected above 550 Hz (see Table 1). Theoretically, Ω depends on the magnetic structure of the neutron star's magnetosphere. In the case of 4U1915-05, there are not enough simultaneous detections of ν_K and ν_h to reconstruct the Ω profile. We thus use the approximation $\Omega = \Omega_0 = const$, as was done also for 4U1702-42 (Osherovich & Titarchuk 1999a). As shown in Fig. 14 (bottom panel), the rotational frequency is indeed consistent with being

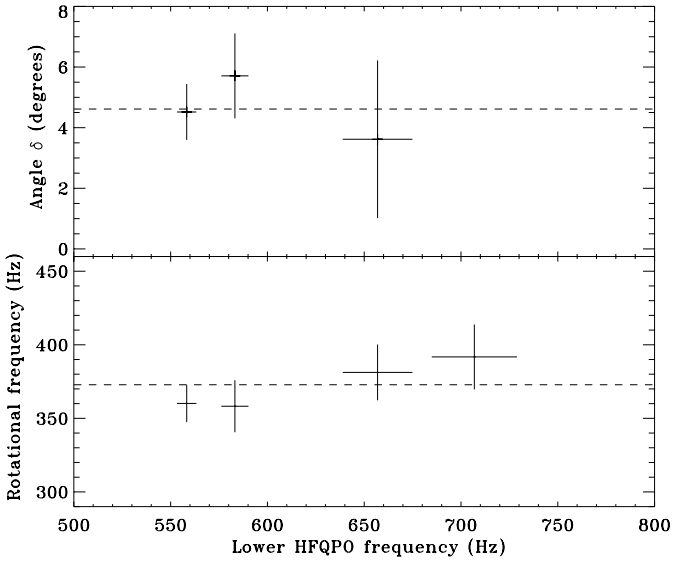

Fig. 14. Inferred rotational frequency (bottom panel) and angle δ (top panel) as a function of the lower HFQPO frequency within the two-oscillator model. The dashed lines represent the mean values. The four points in the bottom panel are inferred from the 4 detections of twin HFQPOs above 550 Hz. The three points in the top panel correspond to the three cases where a LFQPO is simultaneously detected.

constant with $\nu = \Omega_0/2\pi = 373 \pm 36$ Hz. We note that the pair of QPOs at 224 and 514 Hz would correspond to a rotational frequency of 231.2 ± 1.3 Hz inconsistent with the previous value and not considered here.

Knowing Ω, the angle δ can be derived when ν_K and ν_L are measured simultaneously (see e.g. Eq. 5 in Osherovich and Titarchuk (1999a)). The top panel of Fig. 14 shows the inferred angle δ for 4U1915-05, assuming that the LFQPO frequency is ν_L. δ is consistent with being constant with a mean value $\delta = 4.6^\circ \pm 3.1^\circ$. It is in the range of values found for the other sources, but the error is particularly large.

We note however that the relation between Ω, ν_K and ν_h written above requires $\nu_h > 2\nu$, which becomes $\nu_h > 746$ Hz in the case of 4U1915-05. Now, according to Fig. 10 (left) showing the HFQPO frequency as a function of S_a, when only one HFQPO is detected, it seems to be the upper HFQPO. If we assume that it is actually the case and that its frequency is ν_h, then the observed frequency range of ν_h would begin at ~ 500 Hz. This would be inconsistent with the condition $\nu_h > 746$ Hz derived according to the assumptions considered above.

4.5. Implications for the neutron star in 4U1915-05

Observations of HFQPOs allow to derive constraints on the neutron star present in the system. In the framework of beat frequency models, the frequency difference between twin HFQPOs is interpreted as the spin frequency of the neutron star. For 4U1915-05, the mean frequency separation is 348 Hz for four segments of observations. This is consistent with values reported in other LMXBs and would imply a neutron star rotating with a 2.8 ms period. However, a frequency separation of 290 Hz is detected for a pair of QPOs at 514 and 224 Hz. The spin frequency detection at 348 Hz needs to be firmly confirmed.

5. Conclusions

We have analyzed the 1996 RXTE data of the X-ray burster and dipper 4U1915-05. We confirm that it is an atoll source that was probably in its lower and upper banana branch during the RXTE observations.

We report the discovery of both LFQPOs (5-80 Hz) and HFQPOs (200-1300 Hz) and weak evidence for a 0.2 Hz QPO. We show a correlation between the LFQPOs and the HFQPOs frequencies suggesting that both QPOs are produced either by related mechanisms or by the same mechanism seen under different aspects or occuring at different locations in the disk. Furthermore, the LF and HFQPOs frequencies both positively correlate with the position S_a of the source in the color-color diagram that is a key parameter of the timing behaviour though probably not the only one.

Four twin HFQPOs are detected above 550 Hz with a frequency separation consistent with being constant (348 ± 12 Hz) suggesting a spin frequency of 2.8 ms for the neutron star. A pair of QPOs below 550 Hz is also detected with a frequency separation of 290 Hz.

Many more observations have been performed by RXTE. They should help to confirm the picture of the aperiodic variability discovered from 4U1915-05. Especially, the 0.2 Hz QPO and signatures of the neutron star rotation should be searched for in the persistent, dipping and bursting emissions.

Acknowledgements. This research has made use of data obtained through the High Energy Astrophysics Science Archive Research Center Online Service, provided by the NASA-Goddard Space Flight Center. We thank E. Ford and M. Méndez for helpful comments. We are deeply endebted to an anonymous referee for its suitable and detailed comments that helped to improve this paper.

References

Alpar M.A., Shaham J., 1985, Nat 316, 239
Armitage P.J., Natarajan P., 1999, ApJ 525, 909
Barret D., Grindlay J.E., Strickman M., Vedrenne G., 1996, A&AS 120, C269
Barret D., Olive J.F., Boirin L., et al., 2000, ApJ 533, 329
Belloni T., Hasinger G., 1990, A&A 230, 103
Berger M., Van der Klis M., 1998, A&A 340, 143
Bloser P., Grindlay J., Barret D., Boirin L., 2000, ApJ, accepted
Bloser P.F., Barret D., Grindlay J.E., et al., 1996, A&AS 120, C275
Callanan P.J., Grindlay J.E., Cool A.M., 1995, PASJ 47, 153
Chou Y., Bloser P.F., Grindlay J.E., 1999, In: American Astronomical Society Meeting Vol. 195, p. 3911
Church M.J., Parmar A.N., Balucinska-Church M., et al., 1998, A&A 338, 556
Dieters S.W., Van der Klis M., 2000, MNRAS 311, 201
Focke W.B., 1996, ApJ 470, L127
Ford E., 1997, Ph.D. Thesis, Columbia University
Ford E., Kaaret P., Tavani M., et al., 1997, ApJ 475, L123
Ford E.C., Van der Klis M., 1998, ApJ 506, L39
Ford E.C., Van der Klis M., Kaaret P., 1998a, ApJ 498, L41
Ford E.C., Van der Klis M., Van Paradijs J., et al., 1998b, ApJ 508, L155

Grindlay J.E., Bailyn C.D., Cohn H., et al., 1988, ApJ 334, L25
Hasinger G., Van der Klis M., 1989, A&A 225, 79
Hasinger G., Van der Klis M., Ebisawa K., Dotani T., Mitsuda K., 1990, A&A 235, 131
Homan J., Méndez M., Wijnands R., Van der Klis M., Van Paradijs J., 1999, ApJ 513, L119
Homan J., Van der Klis M., Wijnands R., Vaughan B., Kuulkers E., 1998, ApJ 499, L41
Jahoda K., Swank J.H., Giles A.B., et al., 1996, Proc. SPIE 2808, 59
Jonker P.G., Wijnands R., Van der Klis M., et al., 1998, ApJ 499, L191
Kaaret P., Ford E.C., Chen K., 1997, ApJ 480, L27
Kahn S.M., Grindlay J.E., 1984, ApJ 281, 826
Kalogera V., Psaltis D., 2000, Phys. Rev. D 61, 05dc9+
Kamado Y., Kitamoto S., Miyamoto S., 1997, PASJ 49, 589
Kluźniak W., 1998, ApJ 509, L37
Kuulkers E., Van der Klis M., 1998, A&A 332, 845
Kuulkers E., Van der Klis M., Oosterbroek T., Van Paradijs J., Lewin W. H.G., 1997, MNRAS 287, 495
Kuulkers E., Wijnands R., Van der Klis M., 1999, MNRAS 308, 485
Leahy D.A., Darbro W., Elsner R.F., et al., 1983, ApJ 266, 160
Levine A.M., Bradt H., Cui W., et al., 1996, ApJ 469, L33
Lewin W.H.G., van Paradijs J., Hasinger G., et al., 1987, MNRAS 226, 383
Marković D., Lamb F.K., 1998, ApJ 507, 316
Markwardt C.B., Strohmayer T.E., Swank J.H., 1999, ApJ 512, L125
Marshall F.E., Markwardt C.B., 1999, IAU Circ. 7103, 1
Méndez M., 1998, In: Paul J., Montmerle T., Aubourg E. (eds.) Abstracts of the 19th Texas Symposium on Relativistic Astrophysics and Cosmology, held in Paris, France, Dec. 14-18, 1998, (CEA Saclay), p. E348
Méndez M., Van der Klis M., 1999, ApJ 517, L51
Méndez M., Van der Klis M., Ford E.C., Wijnands R., Van Paradijs J., 1999, ApJ 511, L49
Méndez M., Van der Klis M., Van Paradijs J., et al., 1997, ApJ 485 L37
Méndez M., Van der Klis M., Van Paradijs J., 1998a, ApJ 506, L117
Méndez M., Van der Klis M., Van Paradijs J., et al., 1998b, ApJ 494, L65
Méndez M., Van der Klis M., Wijnands R., et al., 1998c, ApJ 505, L23
Miller M.C., 1999, ApJ 520, 256
Miller M.C., Lamb F.K., Cook G.B., 1998a, ApJ 509, 793
Miller M.C., Lamb F.K., Psaltis D., 1998b, In: Scarsi L., Bradt H., Giommi P., Fiore F. (eds.) The Active X-ray Sky: Results from BeppoSAX and RXTE. Proceedings of the Active X-ray Sky symposium, October 21-24, 1997, Rome, Italy, Edited Elsevier, Amsterdam, (Reprinted from: Nuclear Physics B, (Proc. Suppl.), vol. 69/1-3. ISBN: 0444829903.), p. 123
Miller M.C., Lamb F.K., Psaltis D., 1998c, ApJ 508, 791
Morsink S.M., Stella L., 1999, ApJ 513, 827
Olive J.F., Barret D., Boirin L., et al., 1998, A&A 333, 942
Oosterbroek T., Van der Klis M., Kuulkers E., Van Paradijs J., Lewin W.H.G., 1995, A&A 297, 141
Osherovich V., Titarchuk L., 1999a, ApJ 523, L73
Osherovich V., Titarchuk L., 1999b, ApJ 522, L113
Psaltis D., Belloni T., Van der Klis M., 1999a, ApJ 520, 262
Psaltis D., Méndez M., Wijnands R., et al., 1998, ApJ 501, L95
Psaltis D., Wijnands R., Homan J., et al., 1999b, ApJ 520, 763
Revnivtsev M., Borozdin K., Emelyanov A., 1999, A&A 344, L25
Schaab C., Weigel M.K., 1999, MNRAS 308, 718
Schoelkopf R.J., Kelley R.L., 1991, ApJ 375, 696
Shirey R.E., Bradt H.V., Levine A.M., 1999, ApJ 517, 472
Shirey R.E., Bradt H.V., Levine A.M., Morgan E.H., 1996, ApJ 469, L21
Shirey R.E., Bradt H.V., Levine A.M., Morgan E.H., 1998, ApJ 506, 374
Smale A.P., 1998, ApJ 498, L141
Smale A.P., Mason K.O., White N.E., Gottwald M., 1988, MNRAS 232, 647
Smale A.P., Zhang W., White N.E., 1997, ApJ 483, L119
Smith D.A., Morgan E.H., Bradt H., 1997, ApJ 479, L137
Stella L., Vietri M., 1998, ApJ 492, L59
Stella L., Vietri M., Morsink S.M., 1999, ApJ 524, L63
Strohmayer T.E., 1998, In: Accretion Processes in Astrophysical Systems: Some Like it Hot! p. 397
Strohmayer T.E., Zhang W., Swank J.H., et al., 1996, ApJ 469, L9
Swank J.H., Taam R.E., White N.E., 1984, ApJ 277, 274
Sztajno M., van Paradijs J., Lewin W.H.G., et al., 1986, MNRAS 222, 499
Titarchuk L., Osherovich V., 1999, ApJ 518, L95
Titarchuk L., Osherovich V., Kuznetsov S., 1999, ApJ 525, L129
Tomsick J.A., Halpern J.P., Kemp J., Kaaret P., 1999, ApJ 521, 341
Van der Klis M., 1989, In: Ögelman H., Van den Heuvel, E.P.J. (eds.) Timing Neutron Stars. NATO ASI C262, Kluwer Academic Publishers, p. 27
Van der Klis M., 1994, ApJS 92, 511
Van der Klis M., 1995, In: Lewin W.H.G., Van Paradijs J., Van den Heuvel, E.P.J. (eds.) *X-ray Binaries*. Cambridge University Press, p. 252
Van der Klis M., 1999, Proceedings of the Third William Fairbank Meeting, Rome, June 29 – July 4, 1998
Van der Klis M., Hasinger G., Damen E., et al., 1990, ApJ 360, L19
Van der Klis M., Swank J.H., Zhang W., et al., 1996, ApJ 469, L1
Van der Klis M., Wijnands R.A.D., Horne K., Chen W., 1997, ApJ 481, L97
Van Paradijs J., 1995, In: Lewin W.H.G., Van Paradijs J., Van den Heuvel E.P.J. (eds.) X-ray Binaries. Cambridge University Press, p. 536
Vaughan B.A., Van der Klis M., Lewin W. H.G., et al., 1999, A&A 343, 197
Vietri M., Stella L., 1998, ApJ 503, 350
Walter F.M., Mason K.O., Clarke J.T., et al., 1982, ApJ 253, L67
White N.E., Swank J.H., 1982, ApJ 253, L61
Wijnands R., Homan J., Van der Klis M., et al., 1997a, ApJ 490, L157
Wijnands R.A.D., Van der Klis M., Kuulkers E., Asai K., Hasinger G., 1997b, A&A 323, 399
Wijnands R., Homan J., Van der Klis M., et al., 1998a, ApJ 493, L87
Wijnands R., Méndez M., Van der Klis M., et al., 1998b, ApJ 504, L35
Wijnands R., Van der Klis M., Méndez M., et al., 1998c, ApJ 495, L39
Wijnands R., Van der Klis M., 1998, ApJ 507, L63
Wijnands R., Van der Klis M., 1999a, ApJ 514, 939
Wijnands R., Van der Klis M., 1999b, ApJ 522, 965
Wijnands R., Van der Klis M., 1999c, A&A 345, L35
Wijnands R., Van der Klis M., Rijkhorst E.J., 1999, ApJ 512, L39
Wijnands R.A.D., Van der Klis M., 1997, ApJ 482, L65
Wijnands R.A.D., Van der Klis M., Psaltis D., et al., 1996, ApJ 469, L5
Yoshida K., 1992, Ph.D. Thesis, Tokyo University
Yoshida K., Inoue H., Mitsuda K., Dotani T., Makino F., 1995, PASJ 47, 141
Yoshida K., Mitsuda K., Ebisawa K., et al., 1993, PASJ 45, 605
Yu W., Zhang S.N., Harmon B.A., et al., 1997, ApJ 490, L153
Zhang W., Jahoda K., Kelley R.L., et al., 1998, ApJ 495, L9